SANDIA REPORT

SAND2010-6735
Unlimited Release
Printed September, 2010

Computational and Experimental Platform for Understanding and Optimizing Water Flux and Salt Rejection in Nanoporous Membranes

Susan B. Rempe, David M. Rogers, Ying-Bing Jiang, Shaorong Yang, Kevin Leung, C. Jeffrey Brinker, Chris Lorenz, Sameer Varma, Dubravko Sabo, Zhu Chen, Seema Singh, Caroline S. Rempe, Tom Mayer, Todd M. Alam, Peter J. Feibelman, John Merson

Prepared by
Sandia National Laboratories
Albuquerque, New Mexico 87185 and Livermore, California 94550

Sandia National Laboratories is a multi-program laboratory managed and operated by Sandia Corporation, a wholly owned subsidiary of Lockheed Martin Corporation, for the U.S. Department of Energy's National Nuclear Security Administration under contract DE-AC04-94AL85000.

Sandia National Laboratories

Issued by Sandia National Laboratories, operated for the United States Department of Energy by Sandia Corporation.

Available to DOE and DOE contractors from
U.S. Department of Energy
Office of Scientific and Technical Information
P.O. Box 62
Oak Ridge, TN 37831

Telephone: (865) 576-8401
Facsimile: (865) 576-5728
E-Mail: reports@adonis.osti.gov
Online ordering: http://www.osti.gov/bridge

Available to the public from
U.S. Department of Commerce
National Technical Information Service
5285 Port Royal Rd
Springfield, VA 22161

Telephone: (800) 553-6847
Facsimile: (703) 605-6900
E-Mail: orders@ntis.fedworld.gov
Online ordering: http://www.ntis.gov/help/ordermethods.asp?loc=7-4-0#online

SAND2010-6735
Unlimited Release
Printed September, 2010

Computational and Experimental Platform for Understanding and Optimizing Water Flux and Salt Rejection in Nanoporous Membranes

Susan B. Rempe

Abstract

Affordable clean water is both a global and a national security issue as lack of it can cause death, disease, and international tension. Furthermore, efficient water filtration reduces the demand for energy, another national issue. The best current solution to clean water lies in reverse osmosis (RO) membranes that remove salts from water with applied pressure, but widely used polymeric membrane technology is energy intensive and produces water depleted in useful electrolytes. Furthermore incremental improvements, based on engineering solutions rather than new materials, have yielded only modest gains in performance over the last 25 years. We have pursued a creative and innovative new approach to membrane design and development for cheap desalination membranes by approaching the problem at the molecular level of pore design. Our inspiration comes from natural biological channels, which permit faster water transport than current reverse osmosis membranes and selectively pass healthy ions. Aiming for an order-of-magnitude improvement over mature polymer technology carries significant inherent risks. The success of our fundamental research effort lies in our exploiting, extending, and integrating recent advances by our team in theory, modeling, nano-fabrication and platform development. A combined theoretical and experimental platform has been developed to understand the interplay between water flux and ion rejection in precisely-defined nano-channels. Our innovative functionalization of solid state nanoporous membranes with organic protein-mimetic polymers achieves 3-fold improvement in water flux over commercial RO membranes and has yielded a pending patent and industrial interest. Our success has generated useful contributions to energy storage, nanoscience, and membrane technology research and development important for national health and prosperity.

Acknowledgment

We gratefully thank the LDRD program for funding that provided full or partial support to a summer undergraduate student intern, four Sandia postdocs, and three postdocs and a student at the U of New Mexico. We also thank the LDRD office for presenting this project with the 2010 Award for Excellence. Finally, we are indebted to Prof. Eric Jakobsson and a grant from the National Center for Supercomputing Applications at UIUC, which provided compute time to our foreign national postdoc.

Contents

List of Figures

List of Tables

Chapter 1

Introduction

Lack of potable water plagues half the world's population, causing death, disease, and international tension. Furthermore, energy and water are inextricably and reciprocally linked, with production of one requiring use of the other. The best current solution to clean water lies in reverse osmosis (RO) membranes that remove salts from water with applied pressure, but this technology is mature and expensive. Furthermore, the water produced lacks electrolytes important to health. The high cost lies in gathering together and concentrating salt, sodium and chloride ions, by forcing saline water through a membrane to recover purified water on the other side. Incremental improvements, based on engineering solutions rather than fundamental changes to widely used polymeric materials, have yielded only modest gains in reverse osmosis performance over the last 25 years. In order to progress, a breakthrough in materials research is needed.

To achieve a potential breakthrough in reverse osmosis membrane design, we have pursued a fundamental research and development effort that exploits and extends recent advances by our team in theory, modeling, nano-fabrication and platform development. We developed a combined theoretical and experimental platform that enabled us to probe the interplay between water flux and ion rejection in precisely-defined inorganic nano-channels. Inspired by water- and electrolyte-selective protein channels in biological membranes, we investigated the molecular design principles of natural systems that filter water far more efficiently than conventional RO membranes. In contrast to the active site architecture formed by thin dense polymer coatings on commercial RO membranes, biological cell membranes demonstrate fast water flux and selective ion rejection through nanopores at low applied pressure.

With molecular modeling, we identified three key mechanisms used by nature for selecting specific ions for transport across a cell membrane. Each mechanism of selective ion binding shared a common structural feature – binding sites. We found that binding sites composed of dipolar functional groups with specific architectural characteristics can stabilize specific ions for permeation across natural membranes. Furthermore, properties of a binding site can be tuned without changing its structure simply by modulating the charge-response properties of the surrounding environment. Comparison with the crystal structure of biological water-selective channels showed a distinct absence of ion binding sites in the water permeation pathway. Natural water channels instead contain a collection of dipoles, alternating in direction, and mixed with greasy hydrophobic groups lining the channel walls.

Our efforts to transcribe nature's structural design features into robust synthetic porous membranes produced five models of biomimetic pores nanofabricated using self-assembly and novel atomic-layer deposition strategies (ALD). Our experimental and theoretical platforms allowed successive modification of pore size and surface chemistry and charge, followed by measurements of pore structure and selective transport function to deduce structure/transport property relationships in the inorganic nanopores. We found that purely hydrophobic pores, as achieved with trimethyl silane coverage, fully inhibited water transport. As in the natural water-selective channel proteins, partially hydrophilic pore surfaces are required to provide 'binding sites' that stabilize water molecules, increase diffusion, and increase water flux across the membrane. Furthermore, narrow pores with diameters in the nanometer length scale or smaller are required for ion rejection functionality because large pores stabilize ions by permitting counterions and water molecules to permeate with the ions.

Both theoretical and experimental investigations yielded further scientific insights as to the reactivity of titratable walls due to the confining geometry of a nanoporous space. Contrary to the expectation that more confined water in a nanopore exhibits a lower dielectric constant and hence renders the ionization reaction involved in deprotonation of a silanol surface less favorable, ab initio molecular dynamics simulations showed the opposite. Reducing the diameter between two flat walls covered with silanol groups produced a decrease in pK_a, which is associated with enhanced reactivity of the walls.

In the final fabrication of organic modified nanopores by self-assembly and plasma-assisted atomic layer deposition (ALD), we synthesized nanopores with multiple organic surface derivatizations to more closely mimic the structure of water-selective protein channels in cell membranes. In these channels, a polyamide network composed of opposing dipoles from carbonyl and amine groups, with greasy hydrophobic groups in between, stretch across the nanopores. The pores notably lack well-defined ion binding sites characteristic of ion-selective biological channels. Gas permeance measurements confirmed the presence of a nanoporous structure. In a side-by-side comparison of performance between our ALD polypeptide membranes and DOW commercial membranes, the ALD membranes maintained high enough salt rejection to produce drinking water, yet outperformed the commercial membranes by as much as a factor of three in terms of water flux.

Scientific insight gained by establishing structure/transport property relationships in nanopores will inform new membrane processing strategies amenable to economic large-scale manufacturing. With guidance from world-wide experts in macroscopic membranes, our microscopic membranes will have the potential to be scaled up into practical systems that could enhance the quantity of fresh water supplies at an affordable cost for the nation and the world, thus directly furthering Sandia's commitment to water, energy, national security, and public health issues.

A goal of future work is to scale up our system to high-pressure large-membrane formats. Small-scale systems utilizing our novel platform and focusing on transport at the individual pore level are mandatory for design, fabrication, characterization and simulation of the microporous selectivity filter. Similar fabrication strategies can be employed for larger scale anodisc alumina (AO) membranes. During the project, we demonstrated ALD modification of larger-scale, AO-supported mesoporous silica membranes. Surface-confined ALD deposition of a hybrid film followed by removal of the organic template resulted in a microporous membrane with a record high combination of flux and selectivity for gas molecules[9]. Scale-up to technologically-relevant systems requires compatibility with polymeric supports. One approach is the development of reverse phase mesoporous materials, which have organic frameworks and hydrophilic pores. Another is the metal-organic framework materials (MOFs). MOFs spontaneously assemble at room temperature from linkers and connectors much like tinker toys. Their pore size can be tailored by the linker/connector chemistry. MIL-101 and super tetrahedron (ST) MOF have pore diameters of 2.9-3.4 nm and 0.86 nm, respectively. A critical issue is whether MOFs can be prepared as defect-free films. Future scale-up activities can be aided by collaboration with UOP, a leading expert in spiral wound membrane modules, and will include surfactant-templated oxides and ALD deposition on asymmetric cellulose acetate membranes.

This report begins with an analysis of desalination energy requirements in order to quantify the potential for future improvements in desalination membrane technology. The thermodynamic analysis of the first chapter makes it possible to draw conclusions from the vast array of equilibrium molecular dynamics simulations present in the literature as well as create a standardized comparison for measuring and reporting experimental RO material efficiency. Commonly employed methods for estimating minimum desalination energy costs have been revised to include operations at positive input stream recovery ratios using a thermodynamic cycle analogous to the Carnot cycle. Several gaps in the statistical mechanical theory of irreversible processes have also been identified, which may in the future lead to improved communication between materials engineering models and statistical mechanical simulation. Simulation results for silica surfaces and nanochannels are summarized in the following chapter. We next review our progress on experimental design and testing of nanoporous RO materials via templating and atomic layer deposition (ALD). We find that the efficiency of these nanoporous membranes is more than double that of currently available membrane technology for brackish water desalination due to the improved membrane flux and salt rejection at low pressure. Finally, we summarize our conclusions and future work. The creation and evaluation of a novel material platform for RO desalination operating through a templated nanoporous structure has resulted in higher salt rejection at lower applied pressure. This is an important advance because traditional materials operating through diffusion-based mechanisms require high pressures to prevent salt passage.

Full descriptions of the technical and conceptual advances made in this project can be found in a Technical Advance filed with Sandia and articles published in these journals: *J. Am Chem. Soc.*[9, 46, 16, 17], *J. Mol. Biol.*[48], *J. Comput. Theor. Nanosci.*[18, 25], *J. Chem. Phys.*[51, 19, 37], *Nature Materials*[3], *Nature Nanotech*[27], *SMALL*[35], *MRS Bull.*[4], *Phys. Chem. Chem. Phys. (Communication)*[38], *Biophys. J.*[47], *J. Chem. Theory Comput.*[49], *Chem. Phys. Lett. (Frontiers Article)*[2], and *J. Membrane Sci.*[50].

Chapter 2

Thermodynamic Analysis of Membrane Separations Processes

Water permeable, salt excluding membranes carry enormous potential for making drinking water available through reverse osmosis (RO) and generating energy from saltwater mixing through forward osmosis. However, several factors limit the efficiency of the mechanical to chemical potential energy conversion process, including hydraulic pump efficiency, recovery of pressure energy from waste water, uncontrolled mixing of saline and fresh water, and fluid flow resistance of the RO membrane. Along with the thermodynamic cost of solute concentration, these combine to make energy the largest component of the operating cost for seawater desalination facilities[34, 1, 36, 26]. Recent advances in pressure recovery devices have placed the energy conversion efficiency of the mechanical components (hydraulic pump and pressure recovery) in the 85-89% range[42, 1]. Taking example data from the Perth desalination plant[43], the pressure drop across the RO membrane accounts for 1.85 kWh/m^3 of the total desalination energy budget, while 0.4 kWh/m^3 is lost to mechanical efficiency, and a remaining 1.2 kWh/m^3 is used for pre/post treatment and transport throughout the facility.

Comparing the energy cost arising from the membrane pressure drop to the thermodynamic energy cost of 1.1 kWh/m^3 for concentrating dissolved salts in seawater at 44% recovery (calculation method shown in the next section), it is clear that improved membrane materials have a large potential impact on desalination and energy recovery prospects. Typical thin film composite aromatic polyamide with a polysulfone support and asymmetric cellulose triacetate materials have relative resistances of 0.7 and 2.5 $h \cdot bar/cm$[40, 12, 39]. While significant effort has gone into additional treatments to improve these materials, improvements in membrane material performance have been slowing, thus motivating a search for viable alternatives to traditional polymer-based membranes. Zeolite-based membrane materials[23, 22] have been considered, but show too high resistance.

Equilibrium Energy Cost Analysis

RO membranes convert mechanical (pressure) energy into chemical energy by concentrating saline solutions. This section will show a reversible thermodynamic cycle for carrying out this process – relating it to a Carnot cycle where chemical potential is substituted for the heat source. The most important result from this analysis is a lower bound on the energy required for any process used for desalination.

$$\frac{E}{V_{\text{in}}} = RT\left[(1-x)c_o \ln c_o + xc_w \ln c_w - c_i \ln c_i\right] \tag{2.1}$$

In this equation, the process is assumed to use V_{in} m^3 of input water with a solute concentration of c_i moles of solute (or equivalent moles of dissociated electrolyte) per m^3 and produce xV_{in} m^3 of waste water at a concentration of $c_w > c_i$ and $(1-x)V_{\text{in}}$ m^3 of purified water at concentration c_o. Conservation of mass implies the rejection rate is $x = (c_i - c_o)/(c_w - c_o)$, and the recovery rate is $1-x$.

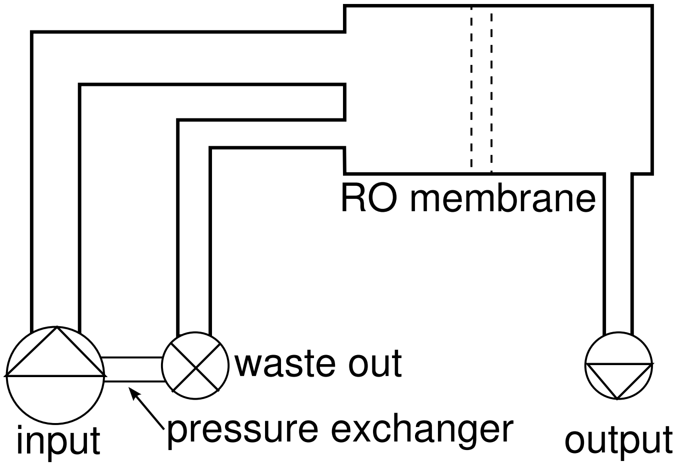

Figure 2.1. Process pipeline for an RO facility. Input water is pressurized using mechanical energy and recycled pressure energy recovered from the effluent stream. It flows to the RO membranes, where the pressure is converted into chemical energy by concentrating the waste-water.

The reverse osmosis membrane operates inside of an industrial process that generates the required work and transports the working solutions. Ideally, all the energy added to the fluid can be recovered except what is consumed by the RO membrane using "perfect" pressure and heat exchangers. In reality, the input pump is only 80-90% efficient, the pressure exchanger is 80-95% efficient, and a steady rate of pressure and heat leakage occurs throughout the pipeline. Current RO desalination plants report that 50-65% of the operating energy (around 2 kW-h / m^3) is consumed in the RO membrane unit[1].

Figure 2.2 shows a cycle operating between two sets of working conditions (input at c_i in the lower half, waste output at c_w in the upper half). A constant total volume V_{tot} is maintained throughout and no expansion / compression of the fluid takes place, so all variables have been made into volume fractions via division by V_{tot}. The cycle begins by

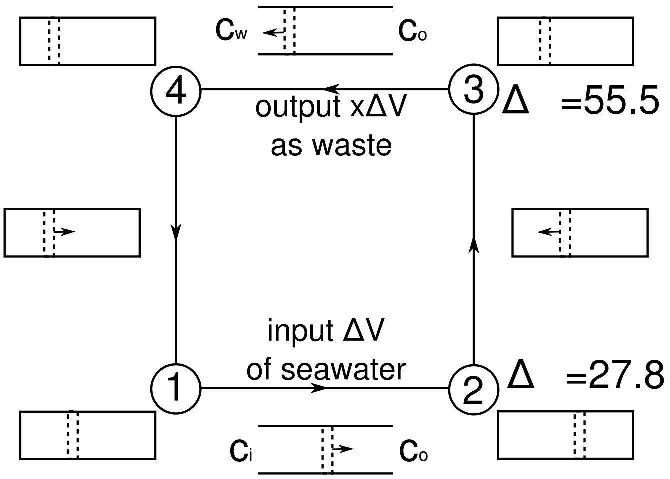

Figure 2.2. Thermodynamic cycle for the RO membrane chemical potential / pressure conversion engine. Osmotic pressure differences are based on seawater to drinking water conversion at 50% recovery.

pulling a volume fraction Δv of input at a constant concentration and osmotic pressure difference – a process requiring zero work, but increasing the potential energy of the enclosed volume. This step is analogous to heat transfer in the Carnot cycle. Next, the left-hand side volume, v_I is compressed, lowering its volume by an amount Δv_c during step $2 \to 3$. A waste volume of $x\Delta v$ is ejected during step $3 \to 4$ (again at constant concentration and osmotic pressure difference), reducing the total desalinated water output of the cycle to $(1-x)\Delta v$. Finally, the input osmotic pressure difference is restored by extracting work from the device.

The eight volume fractions at steps 1–4 can be calculated from four total volume constraints ($v_I + v_{II} = 1$), two number constraints ($N(1) = N(4)$, $N(2) = N(3)$), and the choices Δv, Δv_c. Writing the number constraints as $c_I(n)v_I(n)+c_{II}(n)v_{II}(n) = v_I(n)(c_I(n)-c_{II}(n)) + c_{II}(n)$, $v_I(n)$ are the solutions to four linear equations.

$$\begin{aligned}
v_I(1) &= v_I(2) - \Delta v \\
v_I(2) &= \frac{\Delta v_c}{1-x} \\
v_I(3) &= x v_I(2) \\
v_I(4) &= x v_I(1) = v_I(3) - x\Delta v
\end{aligned} \tag{2.2}$$

These solutions verify the consistency of the above cycle, since a solution exists where all volume fractions are positive when $x \in (0, 1)$.

The energy added to the system during each leg can be computed by assigning a potential energy to each step. To derive this, imagine dissipating all the stored energy from a given state (v_I @ c_I, v_{II} @ c_{II}). This can be done reversibly by allowing the membrane to relax at constant N, giving off work

$$E/V_{\text{tot}} = RT \int_{v_I}^{v_I^f} \frac{c_I v_I}{v} - \frac{c_{II} v_{II}}{v} dv$$

$$= RT \left(c_I v_I \ln \frac{v_I^f}{v_I} + c_{II} v_{II} \ln \frac{v_{II}^f}{v_{II}} \right), \tag{2.3}$$

where $c_I(v) = (c_I v_I)/v$ and $c_{II}(v) = (c_{II} v_{II})/v$ are equal at the point of zero potential energy, $v_I^f = c_I v_I / (c_I v_I + c_{II} v_{II})$. This makes the potential energy of any state equal to

$$E/V_{\text{tot}} = \frac{N}{V_{\text{tot}}} \ln \frac{N}{V_{\text{tot}}} - c_I v_I \ln c_I - c_{II} v_{II} \ln c_{II}. \tag{2.4}$$

The total work required to run the cycle is given by the energy differences $E(3) - E(2) + E(1) - E(4)$ and must balance the "chemical" energy put into the system during the volume flow steps. The energy of the concentration step $2 \to 3$ is

$$E_{2 \to 3}/V_{tot} = \frac{RT \Delta v_c}{1 - x} \left((1 - x) c_o \ln c_o + x c_w \ln c_w - c_i \ln c_i \right). \tag{2.5}$$

This expression also agrees with the energy requirement of a reversible path outlined in Ref. [21], where n_I is held fixed while work is done to vary the volume (solute-impermeable membrane) and then an entropy of mixing is added to make $c_I = c_w$ and $c_{II} = c_o$. It also shows that this step is the only one that must be considered for calculating desalination energy requirements, since its energy is identical to Eq. 2.1 when the output volume $\Delta V (1-x)$ is replaced with Δv_c. Finally, the work released during $4 \to 1$ is

$$E_{4 \to 1}/V_{tot} = RT \left(\Delta V - \frac{\Delta v_c}{1 - x} \right) \left((1 - x) c_o \ln c_o + x c_w \ln c_w - c_i \ln c_i \right), \tag{2.6}$$

proving Eq. 2.1.

As an example calculation, consider a desalination process taking in seawater at 1.12 equivalents, operating at 50% recovery, and producing mineral water at 250 mg/L (6.7e-3 equivalents assuming a KCl standard at 74.5513 g/mol). The waste concentration will be c_w=2.23 equivalents, the osmotic pressure difference at steps 1 and 2 is 27.77 bar and 55.54 bar at steps 3 and 4. In this case, Eq. 2.1 gives an energy requirement of 0.522 kW-h / m^3 of input (1.04 per m^3 of output) at 300 K[1].

We can now apply all the standard efficiency arguments used by Carnot using the reversible cycle above. Importantly, the above represents a maximum efficiency process. To apply the traditional argument, suppose another desalination process were discovered that used less energy than predicted by Eq. 2.1. In this case, we could make most servicable use of its effluent by using it as fuel for running our cycle in reverse. The net work produced in cycle 2.2 would then be greater than was put into the initial effluent production. Equation 2.1 is therefore a theoretical lower limit on the energy requirement of desalination.

---

[1] The thermal energy scale in these units is $RT = 0.69287$ kW-h/m^3 / (mol./L)

If a constant concentration is maintained, and $x \to 1$, L'Hôpital's rule can be used to calculate the limit of Eq. 2.1 divided by $1 - x$ to cast it in terms of output volume.

$$\lim_{x \to 1} \frac{E}{V_{\text{out}}} = RT \left[c_i - c_o \left(1 + \ln \frac{c_i}{c_o} \right) \right] \tag{2.7}$$

This is equal to the usual osmotic pressure difference less a term accounting for the potential energy lost from mixing, causing the process to require less work. For the example above, the extra term is -0.0237 kW-h/m^3, making the total cost at infinitesimal recovery equal to 0.7476 kW-h/m^3.

The reversible thermodynamic cycle of this section shows the connection between alternate ways of understanding osmosis and is closely related to the industrial desalination process. All cycles operating between equilibrium states can be solved by writing out the state functions for each intermediate. This was accomplished here via Eq. 2.4, which can be easily modified for non-ideal osmotic pressure by substituting the equation of state $\Pi(\rho)$ into Eq. 2.3. A connection with the Carnot cycle was made in which it is possible to view desalination as an refrigerator whose coefficient of performance depends on the membrane salt rejection. These results are valid for arbitrary input water recovery ratio, and do not require consideration of vapor equilibria [15].

Energy Costs from Nonequilibrium Transport Theories

Background

In a seminal work by Mr. Staverman in 1951 [41] the linear, local equilibrium approximation of nonequilibrium thermodynamics was applied to the problem of membrane transport in the presence of mechanical (pressure), osmotic, and electrical driving forces. The linear transport theory was unified by Onsager some 20 years earlier [32] and is notable for its ability to synthesize empirical relationships long known to engineering[8]. Pursuing the theory is important, however, since it provides a path toward a nonequilibrium statistical mechanics with which to express transport coefficients from microscopic averages.

The usual Onsager expression assumes the fluxes, j, are proportional to thermodynamic driving forces through the conductivity coefficients, L.

$$\begin{bmatrix} j_S \\ j_W \end{bmatrix} = - \begin{bmatrix} L_S & L_{SW} \\ L_{WS} & L_W \end{bmatrix} \cdot \begin{bmatrix} \frac{\partial \mu_S}{\partial x} \\ \frac{\partial \mu_W}{\partial x} \end{bmatrix}$$

The chemical potential,

$$\beta \mu_i(x) = \ln \frac{\rho_i(x) \Lambda_i^3}{s_i^{\text{int}}} + \beta \mu_i^{\text{ex}}, \tag{2.8}$$

need not be constant throughout the system when it is out of equilibrium. A useful approximation to the chemical potential is given by explicitly considering its voltage and pressure-dependence and then assuming the activity coefficient γ_i is a function of local solution composition only.

$$\begin{aligned} \mu_i &= \mu_i^0 + \beta^{-1}\ln(\gamma_i \rho_i) + q_i\psi(x) + V_i P(x) \\ &\equiv \mu_i^c(x) + q_i\psi(x) + V_i P(x) \end{aligned} \tag{2.9}$$

Assuming no net local charge is built up, voltage differences are approximately zero and don't contribute to the above. Separating the pressure into its own column and writing out the volume flux, $j_V = V_S j_S + V_W j_W$,

$$\begin{bmatrix} j_S \\ j_W \\ j_V \end{bmatrix} = - \begin{bmatrix} L_S & L_{SW} & L_{SP} \\ L_{WS} & L_W & L_{WP} \\ L_{PS} & L_{PW} & L_P \end{bmatrix} \cdot \begin{bmatrix} \frac{\partial \mu_S^c}{\partial x} \\ \frac{\partial \mu_W^c}{\partial x} \\ \frac{\partial P}{\partial x} \end{bmatrix}.$$

This equation defines $L_{SP} = L_S V_S + L_{SW} V_W$ (read across), and $L_{PW} = V_S L_{SW} + V_W L_W$ (read down), etc.

Next, integrate over a line crossing the membrane (assuming constant flux in this direction in the steady-state). This converts the coefficients on the right to average coefficients, and the $\frac{\partial}{\partial x}$-s to Δ-s. According to Ref. [21], the concentration-dependence of the water chemical potential difference is equivalent to $-V_W \Delta\Pi$, the energy difference due to osmotic pressure.

$$\begin{bmatrix} j_S \\ j_W \\ j_V \end{bmatrix} = - \begin{bmatrix} l_S & l_{SW} & l_{SP} \\ l_{WS} & l_W & l_{WP} \\ l_{PS} & l_{PW} & l_P \end{bmatrix} \cdot \begin{bmatrix} \Delta\mu_S^c \\ -V_W \Delta\Pi \\ \Delta P \end{bmatrix} \tag{2.10}$$

Neglecting the contribution to the flux due to the salt chemical potential difference, we get

$$\begin{aligned} j_V &\simeq l_{PW} V_W \Delta\Pi - l_P \Delta P \\ &= -l_P(\Delta P - \sigma\Delta\Pi) \qquad (2.11) \\ \sigma &\equiv V_W l_{PW}/l_P. \qquad (2.12) \end{aligned}$$

This says that the membrane flux is proportional to an effective pressure difference. The effective pressure difference is smaller than ΔP by the Staverman reflection coefficient[41] times the osmotic pressure difference, $\Delta\Pi$. For perfect salt rejection, $\sigma = 1$ and osmosis can take place. If the membrane doesn't reject salt, j_V is less sensitive to $\Delta\Pi$.

To find the relationship between σ and the usual salt rejection, solve for ΔP in terms of $\Delta\mu^c, j_V$ to give an equation equivalent to Eq. 2.10.

$$\begin{bmatrix} j_S \\ j_W \\ -\Delta P \end{bmatrix} = \begin{bmatrix} \frac{l_{SP} l_{PS}}{l_P} - l_S & \frac{l_{SP} l_{PW}}{l_P} - l_{SW} & l_{SP}/l_P \\ \frac{l_{WP} l_{PS}}{l_P} - l_{WS} & \frac{l_{WP} l_{PW}}{l_P} - l_W & l_{WP}/l_P \\ l_{PS}/l_P & l_{PW}/l_P & 1/l_P \end{bmatrix} \cdot \begin{bmatrix} \Delta\mu_S^c \\ -V_W \Delta\Pi \\ j_V \end{bmatrix}$$

Distributing the minus signs and V_W into the coefficients, assuming Onsager reciprocity (i.e. the L matrix is symmetric)[32, 41][2], and substituting the definition of σ, we find

$$\begin{bmatrix} j_S \\ j_W \\ \Delta P \end{bmatrix} = \begin{bmatrix} -\sigma l_S + (1-\sigma) l_{SW} \frac{V_W}{V_S} & -\sigma V_S l_S + (1-\sigma) V_W l_{SW} & \frac{1-\sigma}{V_S} \\ -\sigma l_{WS} + (1-\sigma) l_W \frac{V_W}{V_S} & -\sigma V_S l_{WS} + (1-\sigma) V_W l_W & \frac{\sigma}{V_W} \\ -\frac{1-\sigma}{V_S} & \sigma & -1/l_P \end{bmatrix} \cdot \begin{bmatrix} \Delta \mu_S^c \\ \Delta \Pi \\ j_V \end{bmatrix}$$

To find the salt rejection, we use the concentration of salt in the volume flux at zero osmotic pressure difference.

$$\begin{aligned} \frac{j_S}{j_V} = \frac{1-\sigma}{V_S} &= (1-r)\rho_S^I \\ \Rightarrow \sigma &= 1 - V_S \rho_S^I (1-r) \end{aligned} \tag{2.13}$$

For perfect salt rejection, $\sigma = 1$, while for zero salt rejection, $\sigma = 1 - V_S \rho_S^I$ is less than one – showing a tendancy for the concentrated side to back-flow, diffusing toward the lower osmotic pressure region. However, $V_S \approx 16.6$ mL/mol and a 37 g/L NaCl solution has $V_S \rho = 0.01$. Saturation is about 10× higher, so even at zero salt rejection, the reflection coefficient, σ, cannot possibly drop below 0.9, and is usually higher than 0.99.

Using Eq.s 2.11 and 2.13, the membrane permeability, l_P, can be calculated for experimental data when the applied pressure, salt rejection, and input salt concentration are known experimentally.

At this point it is also possible to set an upper boundary on the permeability by considering the resistance caused by the drag of the rejected ions on the permeant fluid. Because the membrane is hindering the flow of ions, they are moving slower than the surrounding fluid. Collisions will tend to push the ions toward the membrane, while deflected molecules from the permeating fluid reduce the fluid's forward momentum and increase its temperature. When the current has reached a steady-state, the average force exterted by the ion on the fluid will equal the drag force on an ion moved through a stationary fluid. The total drag resistance on a fluid forced to move past n_{bound}/A frozen ions per unit area will therefore be

$$R_{\text{drag}} = \frac{F_{\text{drag}} n_{\text{bound}}/A}{j_V}. \tag{2.14}$$

Diffusion constants, D, for electrolytes in aqueous solutions have been well studied, and are related to the drag force through the friction constant, γ. Requiring balance between external forces and diffusion at equilibrium, Einstein showed $m\gamma = RT/D$. Using the Langevin equation[14],

$$m\tfrac{du}{dt} = R(t) + F_{\text{ext}} - m\gamma u,$$

(where $\langle u \rangle = j_V$, the average flow velocity), it is also possible to show that the solution resistance to an applied electric force leads to a proportionality between the diffusion constant

---

[2] This assumption must hold for infinitesimal deviations from equilibrium, but see Ref. [7] for a counterexample in far from equilibrium conditions.

and the conductivity, Λ [24].

$$D = \frac{RT}{F^2} \frac{\Lambda}{|z|} \tag{2.15}$$

At a steady-state, the number of ions causing fluid drag will remain constant, and $m\gamma\langle u\rangle$ must equal the average force exerted on the ion by the membrane, causing a drag on solution. Therefore

$$F_{\text{drag}} = m\gamma j_V. \tag{2.16}$$

Substituting the density of bound ions times a characteristic height, d, for the layer of bound ions, we arrive at a minimum resistance.

$$R_{\text{drag}} = m\gamma d\rho_{\text{bound}} = \frac{RTd\rho_{\text{bound}}}{D} \tag{2.17}$$

Assuming a boundary height of $d = 10\text{Å}$ and a solute concentration of 0.1 mol/L and using diffusion constants 1.334e-5 and 2.032e-5 cm^2/s for Na^+ and Cl^- leads to a maximum permeability on the order of 10^5 bar·h/cm.

While the CRC Handbook lists ionic diffusion constants at infinite dilution, it is possible to infer diffusion constants in alternate experimental conditions using the Stokes-Einstein relation, $m\gamma \approx 6\pi\eta r$ along with a table of solution viscosities. The viscosity of water at 20°C increases from 1.002 cP to 1.068 cP as the salt concentration increases from zero to 0.7 mol/L NaCl, while a 5° shift to 25°C decreases the viscosity to 0.89 cP[24]. Temperature is thus a much more important factor setting the limiting resistance.

This analysis clearly shows that resistance due to the rejected ions is not a limiting factor as long as they remain in solution near the membrane. However, Chapter 4 gives experimental evidence for the importance of solution boundary layer effects, since doubling the membrane thickness did not lead to the expected 50% decrease in conductivity. Therefore more careful analyses are warranted. Further work using the solution to the Fokker-Planck equations for steady state flux at the experimental membrane geometry may be able to put $d \cdot \rho_{\text{bound}}$ on more quantitative footing.

Standard Test Conditions

Comparing the efficiency of alternative materials for reverse osmosis requires identical flux rates, ϕ_{req}, and salt concentrations $\{c_i, c_o\}$. Under identical test conditions it becomes meaningful to compare the net work done on the fluid, which is governed by the pressure drop across the membrane

$$\frac{E_{req}}{V_{\text{out}}} = \Delta P_{req}. \tag{2.18}$$

Calculating the required energy per unit output at standard conditions requires making two basic assumptions similar in spirit to Ohm's law: the membrane resistance is proportional to both the permeate flux and the membrane thickness.

To relate experimental conditions at constant pressure difference to those at constant flux, we make the assumption that the flux scales linearly with the pressure difference as in Eq. 2.11. Next, use the experimentally observed flux to infer a flux at the required concentration difference by imagining we carried out an identical experiment with α membranes stacked in series so that the "membrane height," L, becomes

$$L' = \alpha L$$

and

$$\begin{aligned} \phi' &= \phi/\alpha \\ l_p' &= l_P/\alpha \\ \frac{c_o'}{c_i} &= (1-r)^\alpha \end{aligned} \tag{2.19}$$

The last equation further assumes that the salt rejection is independent of the input concentration so that, for example, when $\alpha = 2$, then $c_o'/c_i = c_o/c_i \times c_o'/c_o = (1-r)(1-r)$.

For a given $c_{i,req}/c_{o,req}$, we scale the flux by solving for α (assuming the relation holds for concentrations in the range c_o–c_i).

$$\alpha = \frac{\ln c_{i,req}/c_{o,req}}{-\ln(1-r)} \tag{2.20}$$

Now substituting the scaling relation (2.11) in the energy requirement (2.18) and taking the absolute value of all pressure differences gives the energy requirement for carrying out a desalination process at an arbitrary flux, ϕ_{req}, to yield a required osmotic pressure difference, $\Delta\Pi_{\text{req}}$.

$$\begin{aligned} \frac{E_{req}}{V_{\text{out}}\phi_{req}} = \frac{|\Delta P_{\text{req}}}{\phi_{\text{req}}} &= \frac{1}{l_P} + \frac{\sigma|\Delta\Pi_{req}|}{\phi_{req}} \\ &= \frac{\alpha}{l_{P,expt}} + \frac{\sigma|\Delta\Pi_{req}}{\phi_{req}|} \end{aligned} \tag{2.21}$$

Example Application

Mesoporous silica modified by 6 atomic layer deposition (ALD) cycles of trimethoxysilane (TMOS) followed by 16 cycles of aminopropylsilane (APS) deposition to make NH_2 functionalized nanopores has shown rejection ratios around r=31% with a flux around ϕ_m = 1.8 g / cm^2 h. Converting units to a volume flux gives

$$\begin{aligned} \phi\left(\frac{\text{m}}{\text{h}}\right) &= \phi_m\left(\frac{\text{g}}{\text{cm}^2\ \text{h}}\right) \times \left(\frac{1\ \text{L}}{1000\ \text{g H}_2\text{O} + c_o/2\ \text{mol. NaCl} \times 58.443\ \text{g NaCl / mol. NaCl}}\right) \\ &\quad \times 10^{-3}\left(\frac{\text{m}^3}{\text{L}}\right) \times 10^4\left(\frac{\text{cm}^2}{\text{m}^2}\right) \\ &= \frac{\phi_m}{100.0 + 2.922c_o}. \end{aligned} \tag{2.22}$$

Converting the pressure to energy units gives

$$
\begin{aligned}
P\left(\frac{\text{kW-h}}{\text{m}^3}\right) &= P(\text{psi}) \times 6.8947573 \cdot 10^{-2} \left(\frac{\text{bar}}{\text{psi}}\right) \times \left(\frac{1 \text{ kW-h}}{3.6 \cdot 10^6 \text{ J}}\right) \times 10^2 \left(\frac{\text{J}}{\text{L-bar}}\right) \times 10^3 \left(\frac{\text{L}}{\text{m}^3}\right) \\
&= P(\text{psi}) \times 6.8947573 \cdot 10^{-2} \left(\frac{\text{bar}}{\text{psi}}\right) \times \left(\frac{1 \text{ kW-h/m}^3}{36 \text{ bar}}\right) \qquad (2.23) \\
&= P(\text{psi}) \times 1.91521 \cdot 10^{-3} \left(\frac{\text{kW-h/m}^3}{\text{psi}}\right). \qquad (2.24)
\end{aligned}
$$

For $\{c_i = 0.1711, c_o = 0.118\}$ equivalents / L, $\phi = 0.018$ m/h and $\Pi_{expt} = RT \times r \times c_i = 0.03675$ kW-h/m^3 [3]. The flux per over-pressure is $l_P = 0.154$ (indicating that over-pressure must be 6.5 times the flow rate in m/h).

Choosing to run this experiment between concentrations $c_i = 1.12$ and $c_o = 6.7 \cdot 10^{-3}$ equiv./L requires $\alpha = 13.8$ separation stages, and an energy requirement per desired flow rate of

$$\frac{E_{req}}{V_{\text{out}}\phi_{req}} = 89.6 + \frac{0.77}{\phi_{req}}. \qquad (2.25)$$

Based on the form of Eq. 2.21, the minimum required energy is just the osmotic pressure difference as expected, while the flow rate per over-pressure consumes extra energy and lowers the device efficiency. Maximum efficiency would be achieved at zero resistance, where $l_P \to \infty$ and the first term disappears. In this experimental setup, therefore, the efficiency can simply be measured by the ratio α/l_P. To make this independent of the target concentration ratio, we can divide by $\ln c_i/c_o$

$$\epsilon \equiv \frac{\alpha}{l_P \ln c_i/c_o} = (-l_P \ln(1-r))^{-1}. \qquad (2.26)$$

The energy loss Eq. 2.21 can be expressed in terms of ϵ as

$$\frac{E_{req}/V - \sigma|\Delta\Pi_{req}|}{\phi_{req}} = \epsilon \ln c_i/c_o. \qquad (2.27)$$

Eq. 2.27 shows that the energy loss metric, ϵ, can be directly interpreted as a flow resistance for $1 - e^{-1}$ percent rejection.

A plot of ϵ contours vs. r and ϕ_m is shown in Fig. 2.3. The experimental conditions are assumed to be $c_i = 5$ g/L NaCl, $\Delta P = 80$ psi. This plot shows the relative importance of salt rejection and flux on the separation resistance.

Results

In this section, we apply the local equilibrium transport theory of the last two sections to experimental measurements in order to calculate relative material efficiencies.

---

[3] The thermal energy scale at 300 K in these units is $RT = 0.69287$ kW-h/m^3 / (mol/L)

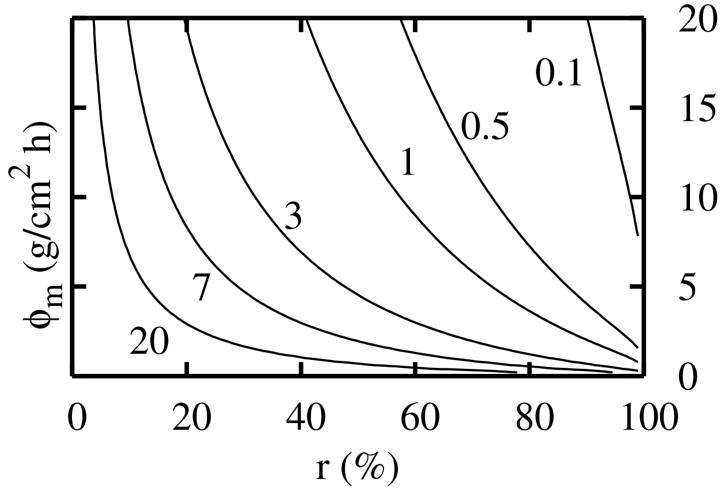

Figure 2.3. Isolines of ϵ, the energy loss per log concentration ratio per required flux as a function of measured salt rejection and mass flux.

Typical performances for asymmetric cellulose di- and tri-acetate membranes have been reported in Fig. 2 of Ref. [12].[4] As the preparations are altered, they find an empirical relationship close to $j_V = -15.14343865r + 16.25638044$ cm/h for pure water permeability and 17 bar operating pressure. Since $V_S\rho_S = 10^{-3}$ is negligible under these conditions, $\sigma \approx 1$ and $l_P \approx 0.956 - 0.891r$. According to the energy loss coefficient,

$$\epsilon = \left(-l_P \ln(1-r)\right)^{-1}, \tag{2.28}$$

the best efficiency point is found at a rejection ratio $r = 0.715$ and permeability $l_P = 0.319$ cm/h-bar, where the standard resistance is $\epsilon = 2.50$ bar/(cm/h). However, no membrane was shown at this point in their diagram, and the closest in efficiency is found to be at a salt rejection ratio of $r = 0.8$, and water permeability of $l_P = 0.256$ cm/h-bar with standard resistance $\epsilon = 2.42$ bar/(cm/h), which is slightly better than the predicted minimum. For a system operating at 30 g/L input concentration (seawater concentration) and 68 bar pressure, the best efficiency was at $r = 0.84, l_P = 0.109$ cm/h-bar and standard resistance $\epsilon = 5.01$ bar/(cm/h).

According to FILMTEC$^{\text{TM}}$[5] materials, SW30HRLE-400 can be run at 32 g NaCl/L and 55.16 bar to get a 99.8% salt rejection at a flow rate of 3.16 cm/h. This implies $l_P = 0.113$ cm/h-bar and $\epsilon = 1.42$. Our tests on FILMTEC$^{\text{TM}}$ polyamide thin film composite (TFC) membrane (SW30HR) at lower concentration and pressure show slightly lower salt rejection,

---

[4] From the data in their Table 3, it can be inferred that the membrane area is 13.2cm^2.

[5] FILMTEC is a registered trademark of FilmTec, a subsidiary of Dow Chemical.

and the FILMTEC^{TM} technical manual notes the output concentration empirically varies inversely to the membrane flux. This cannot possibly hold at low flux though, since then the rejection ratio would become < 0! Our tests carried out at 5 g/L and 13.8 bar give 91% rejection at 0.55 mL/h. Using the Filmtec manual's permeability estimate of 0.279 cm/h-bar, the effective surface area is 0.2 cm^2, and $\epsilon = 1.49$ bar/(cm/h). This is better than the high-salt ϵ because the permeability decreases with added pressure.

Our amide-modified silica nanopores have much larger fluxes. For example the 13.8 bar point above has 86% rejection and a 10.25 cm/h flux (assuming A=0.2 cm^2). These imply a permeability of $l_P = 1.011$ cm/h-bar and standard resistance of $\epsilon = 0.50$ bar/(cm/h). If it could be utilized in current seawater RO plants, the present membrane would drop energy lost due to membrane resistance by 67% – some 0.469 kW-h/m^3, amounting to 26% of the total first-pass membrane-specific energy cost or $1 million/y. for a 100 ML/day RO plant. Presently, however, the burst strength of the silica substrate is not yet high enough to withstand the high-pressure operating conditions required for seawater.

The zeolite membranes reported in Ref. [22] have a rejection of 76.7% and 0.0112 cm/h flux at a salt concentration of 0.1 M NaCl and an applied pressure of 20.7 bar. This gives an anomalously low permeability of 7×10^{-4} cm/h-bar.

The carboxylic acid functionalized carbon nanotube (CNT) reported in Ref. [5] shows a flux of 37 cm/h for a 0.6 mM $K_3Fe(CN)_6$ solution with a pressure of 0.69 bar. Salt rejection for KCl is around 45% at this concentration, while the rejection of the bulkier $K_3Fe(CN)_6$ at this ionic strength is around 98%. Even though this number decreases to zero at concentrations above 10 mM, using these figures gives a permeability of 58.72 cm/h-bar and a tremendous efficiency. However these membranes have not yet shown high enough salt rejection at reasonable operating conditions for brackish water desalination.

Dow maintains a wealth of product information on its website, and summary of membrane permeabilities is given in the Table 2.

The permeabilities found in Table 2, in most cases, are larger than those calculated from the design equations in Table 3.10 of the FILMTEC^{TM} technical manual. For 2, 5, and 32 g NaCl/L salinity these are 0.308, 0.279, and 0.124 cm/h·bar, respectively. This is likely the result of thinner polyamide films employed in brackish water desalination. Unfortunately, there is no test data available for FILMTEC^{TM} brackish water membranes at 5 g/L. However, using the manual's estimate for permeability decrease with increased solution concentration from 2 to 5 g/L, we can expect a 10% increase in the standard resistance, ϵ, over the values listed in Table 2.

Calculations of membrane flux and standardized resistances using the thermodynamic theory developed above have enabled a consistent comparison of membrane materials. In order to decrease the standardized membrane resistance (increasing water permeability), either higher flux or greater salt rejection can be pursued, as shown in Fig. 2.3. Comparing the optimal efficiency for each material gives an indication of the relative performance that can be expected, and shows that current cellulose acetate materials are 2-3 times less efficient

Membrane	Test Salinity (g/L)	Test Pressure (bar)	r	l_P (cm/h-bar)	ϵ (h-bar/cm)	Max Operating Pressure (bar)
XLE-440	0.5	6.9	99.0	0.757	0.287	41
LE-440i	2	10.3	99.3	0.567	0.355	41
LE-440	2	10.3	99.3	0.516	0.391	41
BW30LE-440	2	10.0	99.0	0.534	0.407	41
BW30HR-440i (new)	2	15.5	99.7	0.354	0.487	41
BW30XFR-400/34i	2	15.5	99.65	0.354	0.500	41
BW30-400-FR	2	15.3	99.5	0.328	0.576	41
BW30-365	2	15.3	99.5	0.325	0.581	41
BW30-365-FR	2	15.3	99.5	0.325	0.581	41
BW30-400(also 34i)	2	15.5	99.5	0.323	0.584	41
BW30-440i	2	15.5	99.5	0.322	0.587	41
SW30ULE (new)	32	55.0	99.7	0.167	1.032	83
SW30XLE (new)	32	55.16	99.7	0.137	1.259	83
SW30HRLE (new)	32	55.16	99.8	0.113	1.419	83
SW30XHR (new)	32	55.0	99.82	0.092	1.723	83
SW30XHR	32	55.16	99.8	0.091	1.763	83

Table 2.1. Dow membrane permeability analysis

than polyamide thin film composites, which are on par with our novel nanoporous silica membranes.

Variations in standardized resistances can also be seen when the assumptions (2.19) are violated – that is salt rejection does not remain constant, or the membrane resistance is not proportional to its height. In these cases, we gain information about variations in material formulation that lead to differences in the underlying separation mechanism. Functionalized carbon nanotubes [5] have not produced adequate salt rejection at high ionic strength, which may be explained by a Donnan exclusion mechanism. Polyamide thin film composite (TFC) membranes exhibit increased rejection and resistance at high flow rates and may indicate contraction of the membrane. Directly varying membrane thickness by additional chemical deposition cycles has not lead to a proportionate increase in resistance (Chapt. 4), a fact which points to the importance of concentration polarization at the membrane boundary[28].

Chapter 3

Chemical and Structural Basis for Selectivity and Water Flux

Our experiments show that the behavior of ions confined within nanopores differ significantly from that in free bulk solutions. Our theoretical studies show novel structural designs that control ion passage through membranes. Based on these observations, new ideas will be developed to help us design nanopores that permit fast transport of water and select ions, thus providing novel solutions for energy-efficient highly-selective membrane-based separation technology critical not only to water purification, but also pertinent to electrical energy storage applications in supercapacitors and lithium-ion batteries. Thus our work strongly impacts Sandia's missions in national energy security (efficient separations) and public health (clean, cheap water).

Pressure-Driven Flow

In an important theoretical success, we completed a study of pressure-driven water and salt permeation through model nanopore membranes using non-equilibrium molecular dynamics (MD) simulations[18]. A dual-membrane model is applied, initially with one reservoir filled with 1.0 M NaCl and the other with pure water (see Fig. 3.1). The surfaces of the membrane and the 12 A diameter pore interior are smooth and hydrophilic, and the left-most pore contains a dipolar layer that mimics hydroxylated silica surfaces at the pH of zero charge and electrostatically repels Cl^-[16]. Despite this anion-repulsive surface, at sufficiently high hydrostatic pressure (170 atm.), the membrane only achieves about 32% ion rejection; the ions pass through the pore as Na^+/Cl^- pairs or larger aggregates (Fig. 3.1). At lower pressures closer to the values used in desalination applications (68 atm.), salt rejection is higher, about 70%. This pressure-dependence of salt rejection highlights the importance of moderate pressures for high salt rejection. It also highlights potential pit-falls of MD simulations that apply abnormally high pressures to observe water transport at shorter simulation time scales.

We further decorated the entrance or interior of the dipolar nanopore with $-|e|$ charged spheres to mimic deprotonated carboxylate or silanol groups found in the systems studied experimentally: carbon nanotubes or hydroxylated silica nanopores at neutral pH. Salt rejection ratios are qualitatively similar to those found for the dipolar nanopores (above) at corresponding applied pressures, indicating that the pressure-dependence of salt rejection ratio is a general phenomenon even with decorated pore mouths (Fig. 3.2).

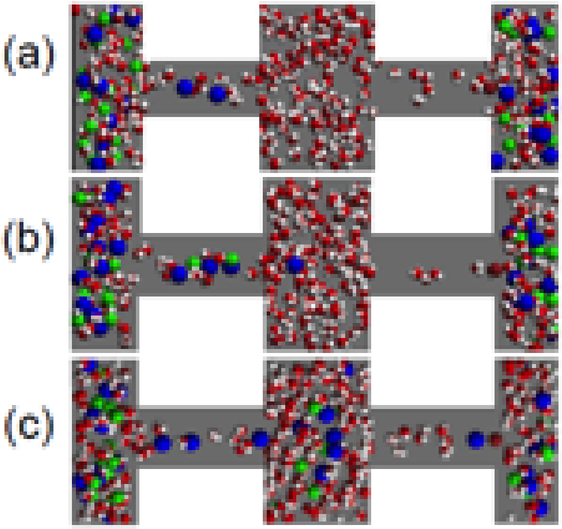

Figure 3.1. NaCl translocation through dipolar nanopores under hydrostatic pressure. Cl^- (green) at entrance, though energetically unfavorable, crosses via ion pair formation with Na^+(blue). (a)-(c): sequential snapshots picoseconds apart. The dual reservoir simulation cell is periodically replicated. H_2O molecules are depicted as red/white spheres.

Effect of Pore Functionality on Ion Rejection

We achieved a significant advance in understanding K^+ over Na^+ selectivity in two diverse biological systems. Theoretical work by us using quantum mechanical models [45] established two essential structural features of a potassium-selective biological ion channel: 1) binding sites that can maintain specific high numbers of oxygen ligands (> 6) for ion coordination; 2) a special local environment (0.5 nm radius) around the binding sites that lacks proton-donor groups, which potentially could compete with a bound ion for its ligands. The high numbers of ligands unexpectedly overcoordinate the permeant K^+ ion, apparently to avoid trapping it. This new mechanistic resolution of cation selectivity has been described as 'the caress of the surroundings, the crowding of the ligands'[11]. Ideas for translating this mechanism into a synthetic membrane pore revolve around the new plasma-assisted atomic layer deposition techniques recently developed by us [10] in conjunction with new molecular imprinting strategies used successfully by us to fabricate sub-nm diameter pores selective to small gas molecules (see below) [9]. We next examined a small molecule with similar

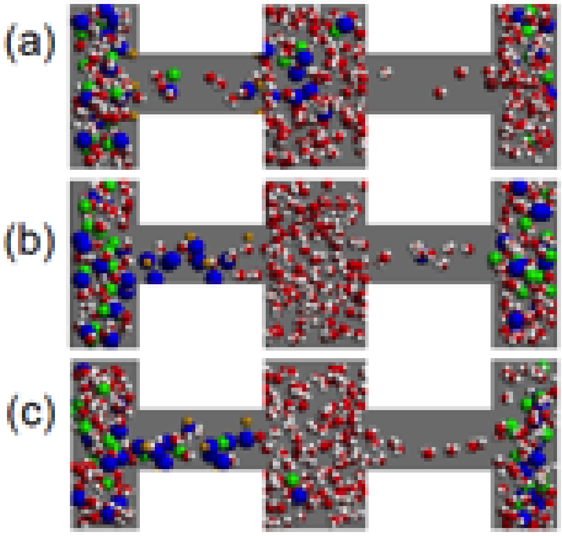

Figure 3.2. NaCl translocation through other types of nanopores, decorated with negative charges (brown spheres) at the pore entrance (a) and in the pore interior (b & c) to qualitatively mimic carbon nanotubes and hydroxylated silica nanopores at neutral pH. In all cases, a high enough hydrostatic pressure causes ion translation in ion pair/larger aggregates. Lower pressures promote ion rejection.

selectivity characteristics toward K^+ over Na^+ ions. This valinomycin molecule binds K^+ with only 6 oxygen ligands. Our work established that valinomycin indeed selects between cations using only 6 ligands. The essential structural feature for valinomycin selectivity is a specific cavity size that fits K^+, not the smaller Na^+[48]. Valinomycin enforces constraints on cavity size using a combination of intramolecular hydrogen bonds and its specific ring size. Compared to the K-channel mechanism, valinomycin tolerates the presence of hydrogen-bond donors in itslocal neighborhood, as is evident from its persistent selectivity in solvents of varying polarity. In addition, its complexation energy with K^+ is small in liquid water, meaning that K^+ ions don't get stuck inside the ring. Thus, we propose that valinomycin's mechanism may work well in a synthetic membrane configuration either directly or through a surrogate molecule. Cheap, simple sugar molecules called cyclodextrins could be encoded with valinomycin's structural features, and plugged into synthetic pores to create K^+/Na^+ selectivity. Cheap ways of incorporating such cation selectivity into desalination membranes can save lives by providing essential minerals to desalinated drinking water.

To investigate the design rules for cation over anion selectivity, we extended our earlier modeling work, which showed the attraction of silica nanopores for Na^+ ions even at the pH of zero charge (PZC)[20]. To begin, we constructed two coarse-grained theoretical nanopore models with smooth hydrophilic pores. One was a tube model of infinite length with alternate dipolar and non-dipolar stretches of length L/2. The other was a membrane model of finite length with dipole layers on the pore interior surface, but not on the membrane surface. As L/2 increases, cations (Na^+) populate the dipolar regions but anions (Cl^-) are excluded (selective cation/anion transport). For the membrane geometry, it is critical that the pore interior surface and the membrane surface have different dipole surface density to achieve selectivity. Total cation/anion rejection can be attained in the tube geometry with alternating dipolar layers. This work [16] suggests a new design for desalination membranes.

Tuning Pore Hydrophobicity and Size

Due to decreased flow resistance, hydrophobic channels are expected to yield a higher water flux than hydrophilic ones. However, hydrophobicity may hinder water entrance and require high pressure to force water through, adding to desalination energy costs. Similarly, larger pore diameters are expected to yield higher water flux, but may lack salt rejection capabilities and hinder water purification.

To investigate the tradeoff between hydrophilic and hydrophobic surfaces, we performed Grand Canonical Monte Carlo simulations to estimate the water content in silica nanopores functionalized with varying amounts of hydrophobic trimethyl silane (TMS, -$Si(CH_3)_3$) groups, each replacing a hydrophobic surface silanol (-SiOH) group. Model silica pores with approximate pore diameters of 10 and 15 Angstroms were created. Periodical boundary conditions were applied so that membrane surfaces are excluded; only interior pore surfaces exist, and 25 and 50% of the SiOH groups therein are replaced with TMS. We found that, at equilibrium, despite the added hydrophobic coverage, the pore interiors are still filled with water in all cases except the 10 A diameter and 50% TMS coverage model. As can be seen in Fig. 3.4, continuous water passageways persist in these pores.

In contrast, full replacement of pore surface silanol groups with hydrophobic trimethyl silane produces a large free energy cost for water occupation. This free energy penalty for the fully hydrophobic pores prevents water entry without an external driving force, and hinders water flux under pressure-driven desalination conditions. Clearly water needs some hydrophilic ‘binding sites’ to be stabilized in a narrow pore. Inspection of the crystal structure of natural water channels (aquaporins) shows they contain a diversity of functional groups on their walls: both hydrophilic polar groups of opposing dipoles (carbonyl and amine) as well as hydrophobic groups. *In Chapter 4, we describe how we translate this functional diversity observed in natural water-selective channel proteins to create pores with both high water flux and high salt rejection.*

Experimental investigations of hydrophobic pores confirm the theoretical predictions. Water flux diminishes to zero as surface coverage with trimethyl silane increases to values greater than 1.5 groups per square nm. Contact angles measured between water and flat silica surfaces show that the angle increases from 38 degrees, for the untreated hydrophilic surface, to more than 90 degrees for trimethyl silane coverages greater than $1.5/nm^2$. Such a larger contact angle represents a repelling capillary force that further increases resistance to water flow. Water flux further diminishes with reductions in pore size. In contrast, salt rejection increases with smaller pores. Theoretical predictions described below correlate smaller water diffusion constants and reduced water occupancy with reduced pore sizes and increased surface hydrophobicity (Fig. 3.3).

Water dynamics in silica pores Fig. 3.4 were investigated using molecular dynamics (MD) simulations. Specifically, two different properties of waters inside the pores were studied. First, the diffusion coefficients $D(z)$ of water molecules were determined as a function of the height along the pore axis, z, using

$$D(z) = \lim_{\Delta t \to \infty} \frac{\left\langle \left(z_i(t + \Delta t) - z_i(t) \right)^2 \right\rangle}{2 \Delta t},$$

where,

$$z - \tfrac{\Delta z}{2} < z_i(t) \leq z + \tfrac{\Delta z}{2}$$

For these calculations, data was analyzed from 10 ns MD trajectories. The bin-width, Δz, was set at 1Å, and the magnitudes of time-intervals Δt were varied from 2 to 100 ps to estimate the $\Delta t \to \infty$ limiting case. Next, water occupancy profiles were estimated by averaging the numbers of water molecules found in each bin during the 10 ns trajectory.

The effect of water force fields on our predictions of water diffusion coefficients and water occupancy in a silica pore was studied by generating three separate trajectories, one using an SPC/E water model, another using a TIP3P water model and the last one using an SPC water model. The silica pore used for this analysis had a diameter of 15Å, and almost half of its pore facing hydroxyl groups (silanol, -SiOH) were substituted with tri-methyl groups (50% hydrophobic with trimethyl silane, $Si(CH_3)_3$). The effect of water force field on the distribution of water molecules inside the pore was negligible, as seen in the occupancy profiles of Fig. 3.5. Each water force field yielded a noticeably different diffusion coefficient profile, but despite the differences, all water models consistently yielded a diffusion coefficient almost an order of magnitude smaller than the diffusion coefficient in bulk water.

Reducing the total number of tri-methyl silane groups on the pore surface to reduce the ratio of hydrophobic to hydroxyl groups from 50% to 25% doubled the diffusion coefficient of water molecules (Fig. 3.6). Nevertheless, the diffusion coefficient of water molecules in the pore still remained small in comparison to their values in bulk water. Reducing the density of hydrophobic groups also increased the occupancy of water in the pore, but this was perhaps because now there was more empty space in the pore due to the substitution of larger $-Si(CH_3)_3$ groups with smaller -SiOH groups. Reducing the pore size, without altering the ratio of tri-methyl over hydroxyl groups (50:50) reduced both the diffusion coefficient and the occupancy of water molecules in the silica pore (Fig. 3.7).

All MD simulations were carried out using the Lammps software. The following parameters were used to carry out simulations in an NVT ensemble: periodic boundaries in all directions; the particle-particle particle-mesh (PPPM) method with a precision value of 0.0001 and a cut-off of 10 for computation of electrostatic interactions; twin-range cut-off of 15/16 for van der Waals interactions; SPC/E charges and van der Waals parameters for description of water models; all atom CHARMM charges and van der Waals parameters for description of silica atoms; an integration time-step of 2 fs; the SHAKE algorithm with a tolerance of 0.0001 units to constrain the Si-O and O-H bonds in silica and all the bonds and angles in water molecules; and a Berendsen method with a coupling constant of 0.1 ps to maintain temperature at 298.15 K.

Further experiments were performed to study how a single hydrophilic functionality correlates with salt rejection and water flux (see also Chapter 4). Samples with -OH surfaces consisted of mesoporous silica, made from Brij-56 lipid later removed with calcination, and then treated to two cycles of liquid-phase atomic layer deposition (ALD) to yield 2.4 nm hydroxylated silica pores. Similar methods were used to generate surfaces with -NH_2, -CN, or -SO_3H functionalized pore surfaces. While nitrile surfaces produced improved water flux and charged surfaces produced higher salt rejection, overall, the singly functionalized hydrophilic surfaces performed modestly in terms of salt rejection and water flux.

To summarize, we find with both experimental and theoretical approaches that some hydrophilicity is required on the walls of nanopores to permit spontaneous water filling. More hydrophilicity is associated with higher water occupancy, higher water diffusion constants (but still smaller than in bulk liquid water), and experimental observations of higher water flux. While larger pores also yield higher water flux, salt rejection is diminished. Small pores functionalized with a single type of hydrophilic coating generally yield modest salt rejection and water flux and thus highlight the subtle design requirements used by natural pores to achieve both fast water transport and perfect salt rejection.

Salt Concentration and pH Dependence

In this section we describe observations of surface-charge-dominated ion transport through silica nanopores at very low salt concentrations. Surface charge plays an important role in ion transport through nanopores with pore sizes smaller than the Debye screening length (λ). We also observed that for pure HCl solution at pH=3, 4 or 5, where ion transport is expected to be dominated by surface charge instead of the bulk solution ion concentration, the ion conductance, and hence the silica surface charge at pH=3, is always higher than those at pH=4. In contrast, on flat silica, the surface charge at pH=4 should be higher because the zero-surface-charge point (isoelectric point) for silica surface is at pH=2. We hypothesize that the isoelectric point of silica may be shifted to higher values in nanopores. Direct measurement of surface charge shows that the isoelectric point (a pH value for zero surface charge) of the silica nanopore surface has shifted to higher pH values compared to a free flat silica surface (Fig. 3.8).

The ion current through nanopores was measured at different salt solutions using a patch-clamp system on a nanofabricated platform comprising a 50-100 nm aperture milled by focused ion beam (FIB) and a 30-50 nm thick tunable mouth self-assembled nanoporous (<3nm) layer coated on the FIBed aperture. We observe two unusual behaviors significant to desalination performance. 1) When the pore size is comparable to the Debye screening length for various salt concentrations, the ion currents at low concentrations are higher than what we expect from a linear model (Fig. 3.9(a)), suggesting that the counter ions attracted by the inherent pore surface charge to the pore surface vicinity is the main mechanism for ion transport. 2) Based on a Debye length of 1.0 nm for a bulk solution of 0.1 M KCl, the screening region should have occupied much of the pore (pore size =2.6 nm), and a transition point to surface-charge-dominated ion transport should be observed at 0.1 M concentration. Instead we observed a transition point at ∼0.01 M, suggesting that the Debye length inside the 2-3 nm nanopore is smaller than that for a free bulk solution (Fig. 3.9(a)). We hypothesize that the isoelectric point (a pH value for zero surface charge) of the silica nanopore surface has shifted to higher pH values compared to a free flat silica surface.

To follow-up on this hypothesis, zeta potentials (an indication of surface charge) of non-porous silica were measured at different pH (see Fig. 3.8a) The results show that the isoelectric point for nanoporous silica is at pH=3-4, in contrast to pH=2.5 for a flat silica surface. This result has been further confirmed by the KBr adsorption of nanopores at different pH. Fig. 3.8b shows the EDS elemental analysis for CTAB mesoporous silica film soaked with KBr solution at different pH (adjusted by HCl addition) then air-dried. At pH=3, the adsorbed ions are mainly negative (e.g. Cl^- from HCl; Br^- from KBr), indicating a positive surface charge at pH=3; at pH=4, K^+ starts showing up, indicating the transition to negative surface charge; at pH=5, no Br^- was found, indicating a negative surface charge. To summarize, a narrow pore geometry can facilitate salt transport at very low concentrations because ions interact with the charged surfaces, while transition to a constant salt rejection regime occurs at a smaller than expected Debye screening length. The shift in isoelectric point reflects new behavior of titratable silica surfaces in a nanoporous geometry: compared to bulk silica, negatively charged surfaces can be neutralized with fewer protons added to solution. These studies provide us with an understanding of pore properties that can help us design energy-efficient water channels.

Origins of the Dual Acidity Observed in Silica Membranes

In a major theoretical advance, we identified the structural origins of the dual-acidity constant behavior observed at silica-water interfaces[17]. Ref. [31] reported that 19% (81%) of surface SiOH groups exhibit pKa=4.5 (8.5), respectively. This acid-base behavior governs the net charge inside silica pore membranes, which in turn affects desalination performance. As silica-water interfaces tend to be amorphous and difficult to image, we have applied accurate ab initio molecular dynamics simulations to compute the free energy of silanol group acidity in diverse chemical and hydrogen-bonding environments. We find that most models proposed for the two pKa's in the literature, such as those based on chemical connectivity and inter-silanol hydrogen bonding motifs, all yield pKa 7.9-9.5. High acidity of pKa 4.5, which approximates that of acetic acid (vinegar), is observed only on strained/defected regions of silica surfaces, on which we also find evidence of water-incorporation reactions.

We also examined the pKa of narrow silica slits to compare with the shift in pH of zero charge (PZC) measured in experiments. 3, 4, and 6 layers of water are confined between periodically replicated β-cristobalite slabs with reconstructed (100) surfaces, yielding 4.0 surface SiOH groups per square nanometer of silica surface. AIMD simulations were applied to calculate the deprotonation potential of mean force (Fig. 3.10) and extract the pKa. We found that SiOH groups in very narrow water-filled silica slits, containing only 3 and 4 layers of water, yield a pKa of 6.9. With approximately 6 layers of water, pKa=8.0 is predicted. Thus reducing the slit width actually decreases the pKa. This is contrary to the expectation that more confined water exhibits a lower dielectric constant and hence renders the ionization involved in deprotonation less favorable. In other words, a higher pKa is expected for more confined water and our experimental measurements of refractive index inside the silica nanopores do indicate a reduction relative to bulk water. However, all predicted pKa exhibit a standard deviation of about 0.5 pH unit. Hence one may argue that all the pKa in Fig. 3.10 are within statistical uncertainties of each other.

Compared to experimental results described earlier, we note that our model silica slits exhibit confinement in one dimension and do not have a cylindrical geometry. Furthermore, the experiments measure the PZC, which is the arithmetic mean of the pKa of -SiOH and $SiOH_2^+$. Therefore the simulations and experimental results are not directly comparable.

Discussion

Our theoretical and experimental platforms enable us to investigate the interplay between water flux and ion rejection in precisely-defined nano-channels. Our simulation studies of ion rejection reveal that high pressures can force salt pairs into a channel, even if the channel is functionalized with charged groups at the entrance or interior. This highlights potential pitfalls of molecular simulations that apply abnormally high pressure in order to observe water transport at short simulation times and may also highlight difficulties with operating desalination plants at high pressures. Theoretical studies of natural channels reveal three sets of design rules for specific ion selection (at appropriate pressures) that could generate more healthy drinking water as well as provide input to a variety of industry and energy applications. Propositions for translating these ion-selective design features to inorganic pores have been made, but not yet tested. Instead, we pursued a systematic experimental and theoretical investigation to determine how variations in the chemistry of the nanopore walls and their size affect water flux and salt rejection. Although varying levels of hydrophobicity using TMS produced only modest flux and ion rejection performance, we learned important lessons regarding hydrophobicity and pore size: 1) Some hydrophilicity on channel walls is required to provide stabilizing water 'binding sites;' and 2) Small pore size enhances ion rejection commensurate with reduction in water flux.

In biological channel proteins, water-selective pores with perfect salt rejection are composed of narrow (sub-nm) pores that pass water fast and in single file. These pores lack the architectures associated with ion selectivity. Furthermore, narrow 'selectivity filters' are also associated with fast (selective) ion transport. An investigation into the properties of small pores reveals the importance of ion-surface interactions on ion transport properties. The Debye screening length for a solution of specific salt concentration inside a 2-3 nm nanopore is smaller than expected (relative to bulk solution). Therefore ion transport mechanisms are dominated by interactions with charged surfaces even at low concentrations and lead to enhanced ion transport. Further investigation into the charge of the confined silica surfaces shows that charge in relation to solution pH is not as expected. In the nanopore geometry, direct measurement of surface charge shows that the isoelectric point (the pH value for zero surface charge) is shifted to higher pH values relative to a flat surface. Thus, smaller additions of protons (smaller shifts in pH) change the surface from negative, to neutral, to positive. With theory, we investigated the structural origin of acid dissociation constants of the hydroxylated silica surface and determined that strained regions of silica surfaces incorporate water and yield more reactive (more readily dissociable, more acidic, lower pK_a) surfaces. Thus, to approach the biological properties of cell membranes that we wish to mimic initially, that is, the fast water transport and high salt rejection of the water-selective protein channels, we conclude that we should avoid overly high pressures, avoid dipole arrangements on the pore walls that produce ion binding sites, and create narrow pores that promote interactions between surface and permeating species.

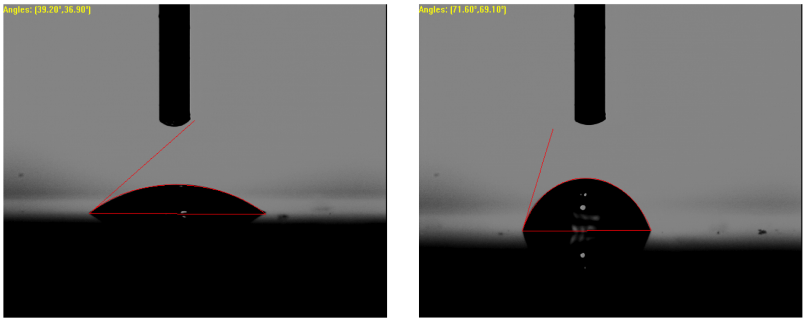

(a) Unmodified silanol surface, C.A.=38°

(b) Treated at 150°C to yield 1.0 TMS/nm^2, C.A.=70°

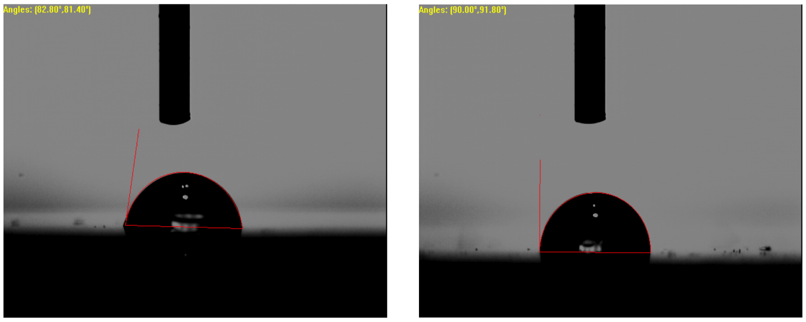

(c) Treated at 200°C to yield 1.3 TMS/nm^2, C.A.=82°

(d) Treated at 250°C to yield 1.6 TMS/nm^2, C.A.=91°

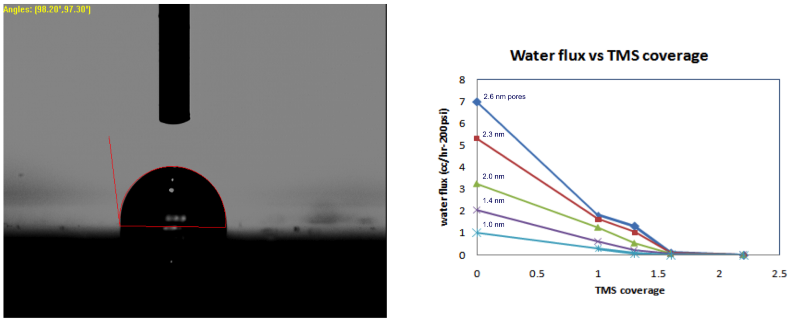

(e) Treated at 300°C to yield 2.2 TMS/nm^2, C.A.=98°

(f) Membrane flux

Figure 3.3. Variation in water contact angle (CA) and channel flux with surface hydrophobicity (obtained by treating surfaces with trimethyl silane, TMS). Water flux diminishes with reductions in pore size (f) and increased hydrophobicity.

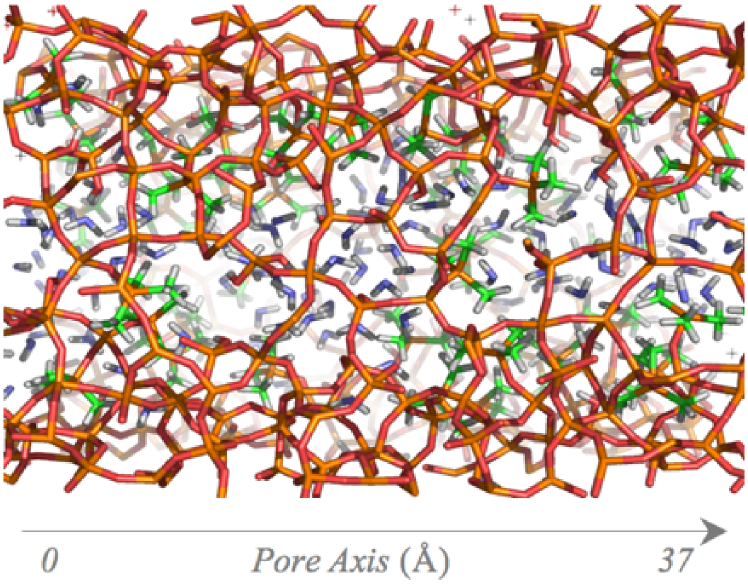

Figure 3.4. Representative snapshot of a silica pore simulated under periodic boundary conditions. The Si atoms are colored orange, the O atoms of silica are colored red, the C atoms of the methyl groups are colored green, the O atoms of the water molecules are colored blue, and all H atoms are colored white.

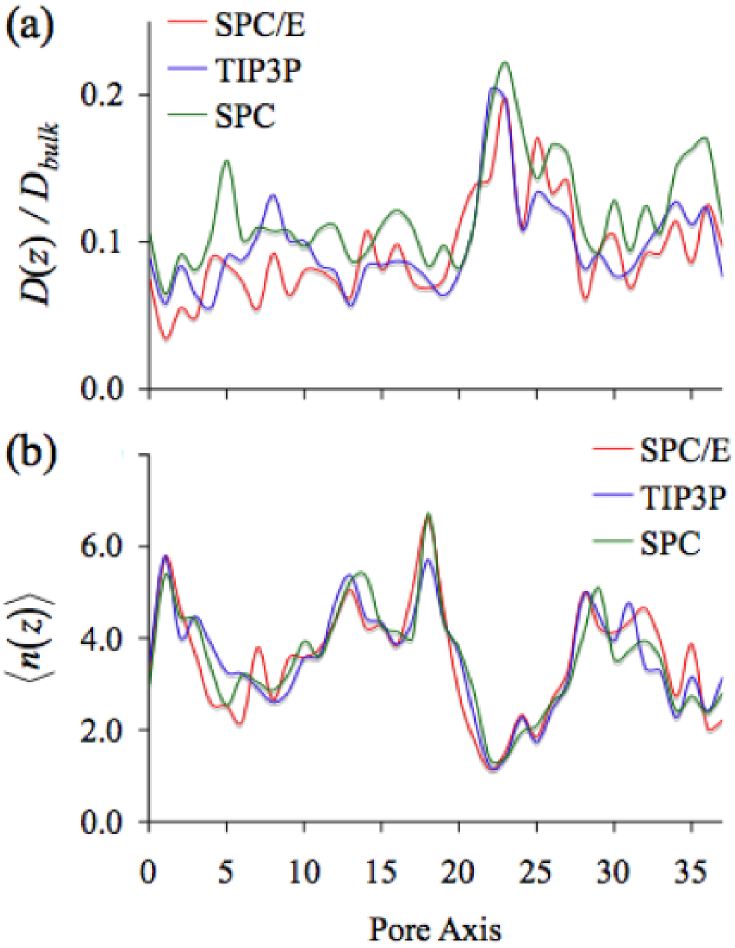

Figure 3.5. Effect of water force fields on the diffusion coefficients (top) and occupancies of water molecules (bottom) inside silica pores

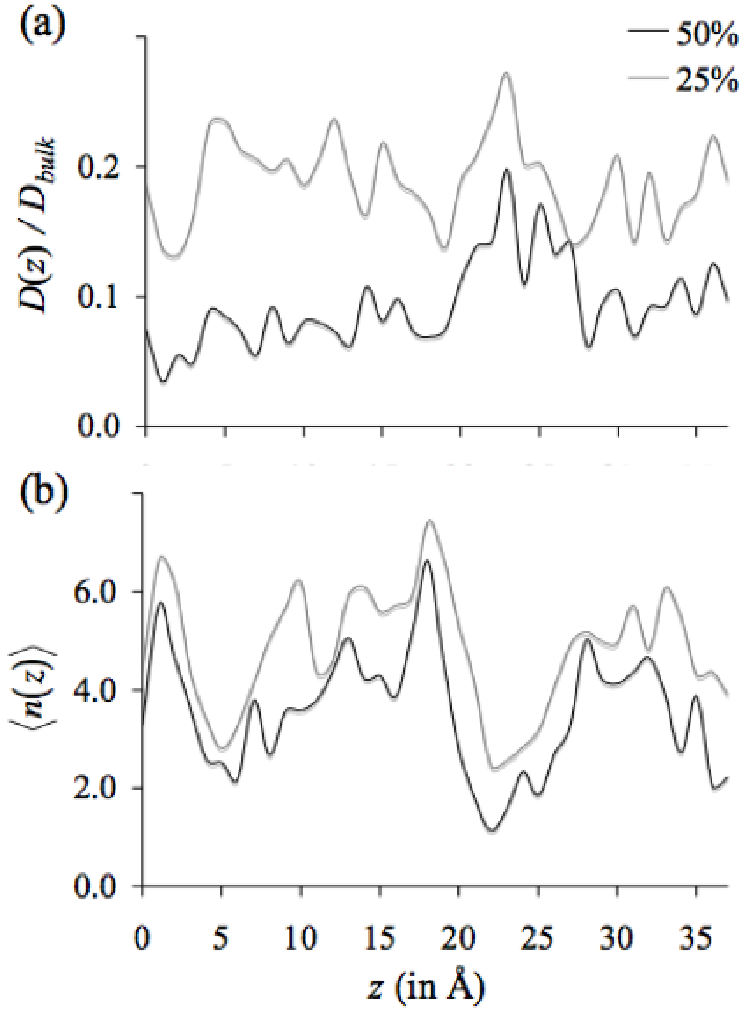

Figure 3.6. Effect of the degree of methylation on the diffusion coefficients and occupancies of water molecules inside silica pores

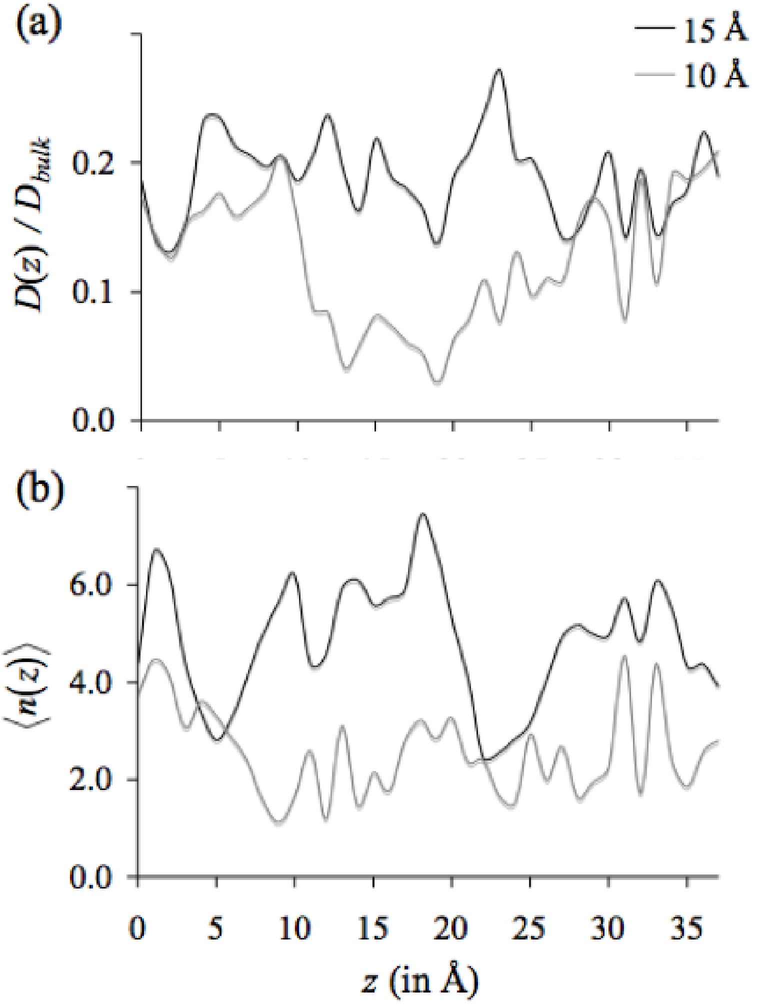

Figure 3.7. Effect of pore size on the diffusion coefficients and occupancies of water molecules inside silica pores

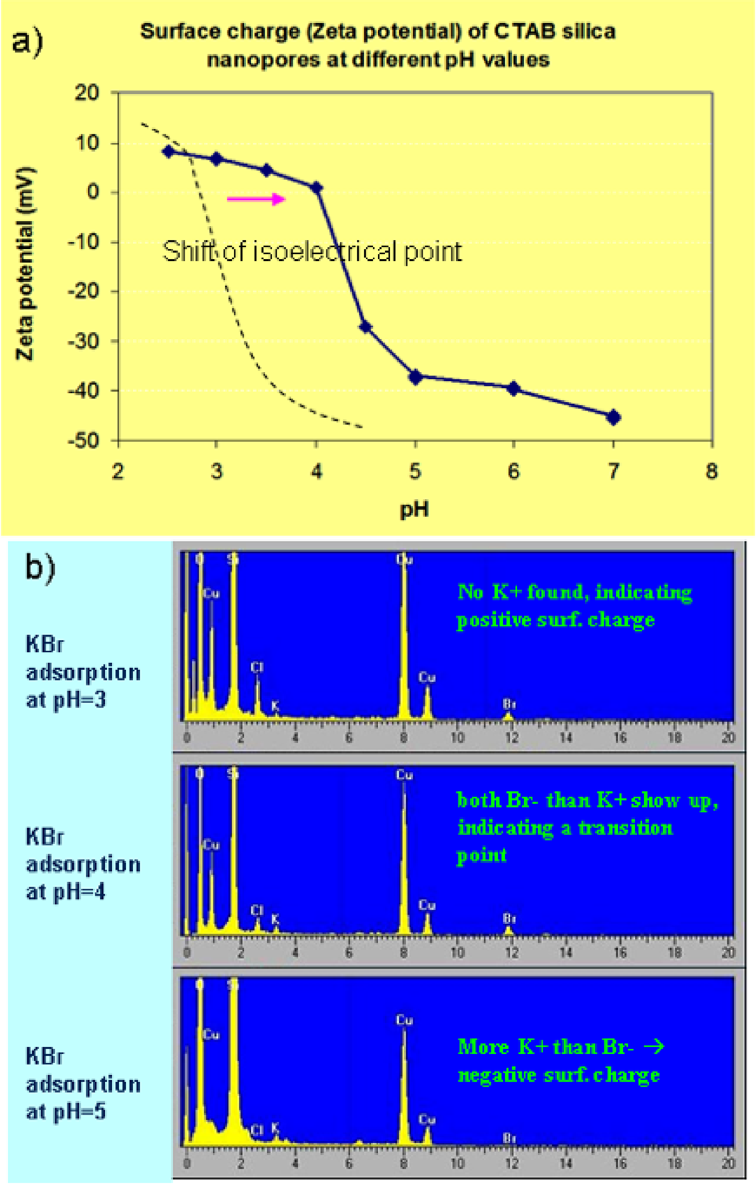

Figure 3.8. a) Zeta potential measurement of mesoporous silica; b) EDS data of KBr adsorption in mesoporous silica as pH varies.

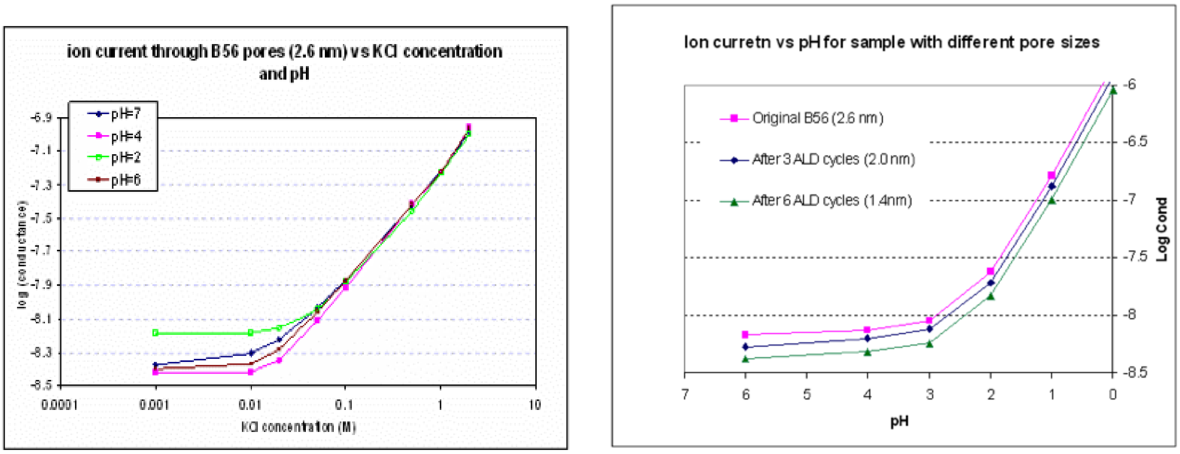

(a) Effect of salt concentration on 2.6 nm B56 pores

(b) Effect of pH on pores of varying diameter

Figure 3.9. Effect of salt concentration and pH on ionic current through silica nanopores.

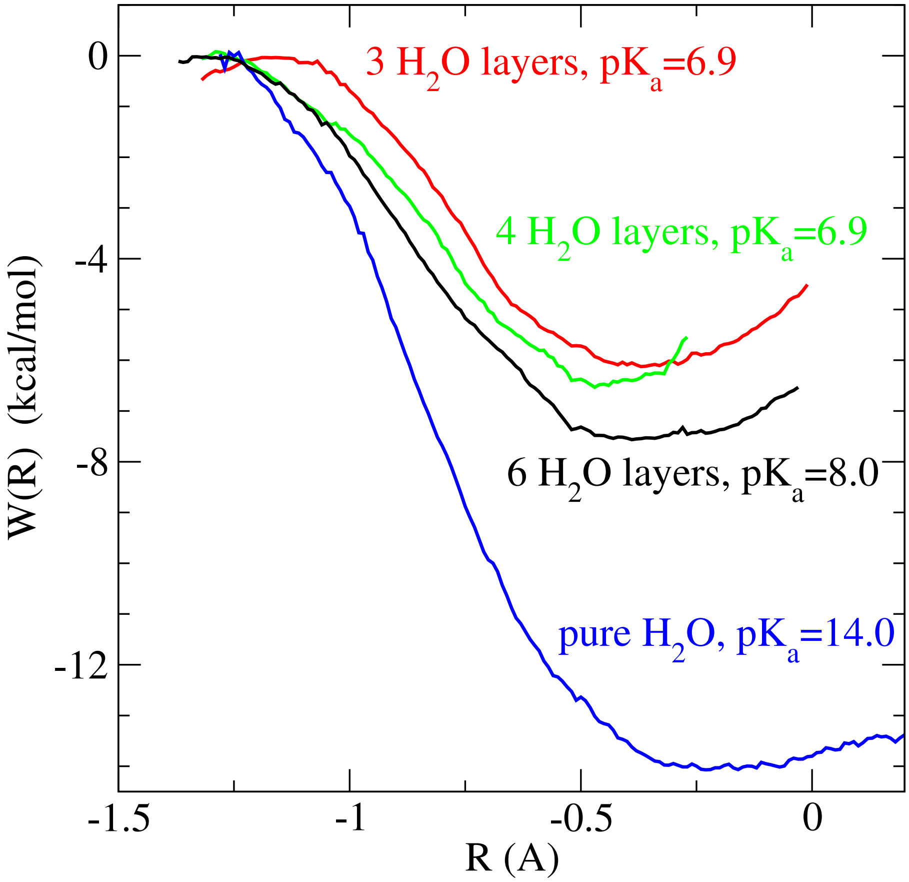

Figure 3.10. Deprotonation potential of mean force and pKa as functions of the approximate number of water layers confined between silica slabs.

Chapter 4

Biomimetic High-Flux Desalination Membrane Based On Self-Assembled Nanopores Tuned by Atomic Layer Deposition

At present, an important application area of RO technology is desalinating brackish water from interior sources that are in the range of 3–16 g/L[26]. Although less pressure (and energy) is required for these input sources, traditional diffusion-based membrane materials require high flux in order to maintain acceptable salt rejection. A membrane material able to maintain high rejection at low flux rates is required for a breakthrough in this application. Toward this end, we report here our investigation of nanoporous separation membranes.

Porous aluminosilicates are well-known, roughly hexagonal structured, alternatives to zeolite materials[13] that can be functionalized by grafting surface silicates as in standard reversed-phased liquid chromatography column preparation. Aluminosilicate membranes containing pores around 20 nm in diameter and occupying 25-50% of the surface area formed the starting point for our experiments. A regular, oriented substructure composed of 2.6 nm pores was then formed with a solution of silica and Brij-56 lipid followed by calcination to remove the lipid. Finally, functionalization proceeded via deposition of silanes and layer-by-layer coating growth during liquid-phase atomic layer deposition (LP-ALD) reaction cycles. The molecular channels in the resulting peptide network have a sub-nm diameter with exposed -N-H, O=C-, and hydrophobic aromatic groups, deliberately designed to mimic the surface chemistry found in biological water-selective channel proteins.

The salt rejection and membrane flux were characterized for varied surface chemistries and pore sizes. We found that the salt rejection of porous ALD membranes increases substantially after ALD modification with alternating amine and hydrophobic chemistries. After 32 ALD cycles, these membranes show 85-95% salt rejection and more than triple the water flux of a polyamide thin film composite (TFC) membrane designed for seawater desalination. In addition the ALD membrane retains its high salt rejection properties at low pressure ranges (<150psi), suggesting a novel rejection mechanism able to operate efficiently at low applied pressure.

Because of the oriented channel architecture afforded by our experimental platform, it is interesting to compare the pore structure with the naturally occurring aquaporin water channel. Aquaporins allow water transport at rates on the order of 10^9 molecules per pore per second and complete rejection of ions[6, 44]. Structurally, each aquaporin channel consists of six transmembrane α-helices arranged in a right-handed bundle to form a narrow channel. A series of backbone carbonyl oxygens, each providing a high dipole moment of around 3.5 Debye, line one side of the channel and accept one hydrogen bond per water to properly orient a chain of translocating waters. The other side is composed primarily of hydrophobic, aromatic residues (one phenylalanine, and several tryptophan side-chains). This regular structure is interrupted in the middle by the asparagine NH_2 functional groups of two NPA (asparagine, proline, alanine) motifs donating hydrogen bonds in order to prevent proton conduction. The narrowest segment of the channel has a constriction between 3 and 5Å in diameter[29, 44].

Similar to aquaporins, our synthetic nanopores contain both hydrophilic amide and hydrophobic aromatic functionality within a similar pore radius. However, ALD is not able to achieve the same level of structural control over the pore geometry. Thus water molecules translocating through the synthetic channel experience pockets of aquaporin-like functionality, but are not as structurally constrained into a stable, ordered, single-file line.

Materials and Methods

The desalination membrane was fabricated by coating self-assembled mesoporous silica on 13 mm diameter anodized porous alumina discs (anodiscs®[1]) from Whatman, followed by progressively tuning pore size and surface chemistry via atomic layer deposition.

To prepare mesoporous silica, 0.90 g of Brij 56 was dissolved in 15 mL ethanol, followed by addition of 2.8 g of tetraethoxysilane (TEOS) and 1.25 mL of 0.07 M HCl aqueous solution. The solution was stirred vigorously for 75 minutes then diluted with water to 65 mL. Anodiscs® were then dip-coated using this solution twice, and the dip-coated samples were calcined at 450°C for 3 hours.

In order to provide anchoring functionality for the ALD reactions, amine groups were added to the silica surface by immersing samples in a toluene aminopropyl triethylsilicate (APS) (33% w/w) and triethylamine (3% w/w) for 2 hours. The residual APS was removed under vacuum at 100°C, and confirmed with FT-IR (Fig. 4.1).

ALD was carried out at 120°C in an Å-dep ALD system. Terephthaloyl chloride (TC, heated at 120°C), triethylamine (TEA) and parabenzenediamine (PA, heated 120°C) were used as the precursors. Each ALD cycle consisted of the following four steps: 1) 20 seconds exposure of TC and TEA; 2) Ar purge at a flow rate of 10 sccm for 10 seconds; 3) 20 seconds exposure of PA and TEA. 4) Ar purge at a flow rate of 10 sccm for 10 seconds.

---

[1] Anodisk is a registered trademark of Whatman Int'l Ltd., UK

These steps were repeated to achieve surface polymer growth, progressively shrinking the mesopore radius.

Results and Discussion

Fig. 4.1 shows the FTIR spectra for the mesoporous silica samples treated by APS with various reaction times. We assigned the absorption at 1070 cm^{-1} to the Si-O stretching vibration; the absorption at 3600 cm^{-1} to surface silica -OH groups; and the absorptions at 2800 cm^{-1} and 3300 cm^{-1} to C-H and N-H stretches, respectively. Because the absorptivity of the N-H bond is low, only a small peak is visible at 3300 cm^{-1}. The C-H signal at 2800 cm^{-1} can be attributed to the CH_2 group in the -CH_2-CH_2NH ligand, and confirms modification of the pore surface by APS.

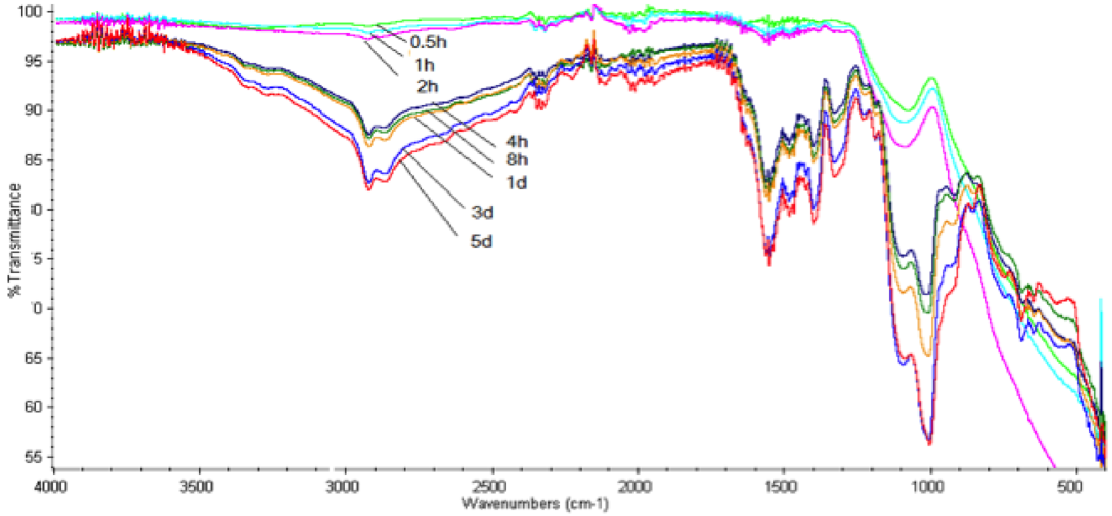

Figure 4.1. FTIR-ATR Spectra for APS Pretreatment of Anodiscs®

Fig. 4.2 shows the FTIR spectra for the samples before ALD modification (the red spectrum), after 8 cyles polyamide ALD (the purple spectrum) and after 32 cycle polyamide ALD (the blue spectrum). Before ALD, there was no substantial absorption in the range of 1200-1900 cm^{-1}. At 8 cycles of ALD, strong signals at 1680 cm^{-1} and 1510 cm^{-1} are present. These are characteristic of amide I bond and amide II bonds, respectively. The adsorption at 1440 cm^{-1} and 1285 cm^{-1} can be attributed to N-H deformation and C-N stretch in amide structure. After 32 cycles of ALD the intensities of all these peaks increase, indicating continued deposition of polyamide in agreement with our observations of decreased pore radius.

In order to probe the progressive pore size reduction by ALD modification, the membrane's permeability to N_2 and He was studied. Fig. 4.3(a) shows the gas permeance of

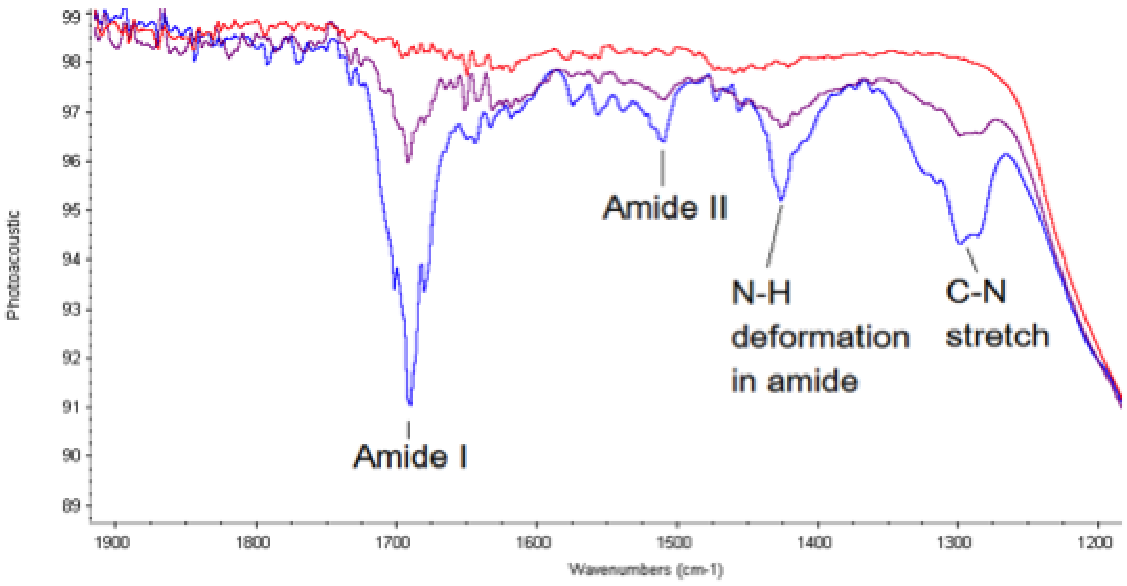

Figure 4.2. FTIR spectra of samples before and after ALD

membranes after various ALD cycles. Prior to ALD, the membrane showed good permeability to both N_2 and He, and the He/N_2 selectivity was about 2.0. This is in agreement with Knudsen diffusion operating at a pore size of 2.6 nm, much larger than the molecular diameters of both N_2 (3.6Å) and He (2.2Å). When the number of ALD cycles increases, the permeance of both N_2 and He decreases, confirming the progressive pore size reduction. In this range, the permeance is proportional to the square of pore diameter, as predicted by Knudsen diffusion with a cylindrical pore model. After 8 cycles, the He/N_2 selectivity becomes > 2.6. This suggests that the gas transport mechanism has changed from Knudsen diffusion to configurational diffusion,where the pore size is expected to be about 3–4 times the gas molecular diameter, or 1.0–1.4 nm. After 16 cycles, N_2 permeance tends to zero, indicating that no pores larger than 3.6 Å remain. This implies an ALD deposition rate of about 0.08 Å/cycle or higher (if extra cycles were required to close unsealed defects generated during the Brij-56 templating). At this moment, the He permeance is still about 6.4 sccm/bar, suggesting that the membrane still has an atomic scale pore size of about 2.2–3.6 Å, considering a He molecular diameter of 2.2 Å. After 32 cycles, the He/N_2 selectivity increased to 36 and He permeance was 4.8 sccm, showing that the membrane retains some porosity with pore diameter around 2–3 Å.

After LP-ALD deposition of polyamide, water permeance and salt rejection properties were measured using an *Alltech* high pressure HPLC water pump, with a constant input feed at 5 g/L NaCl solution and an imposed membrane pressure drop of 200 psi. Figure 4.3(b) shows the water flux and salt rejection of the membrane samples described above. Before ALD modification, the pore size was 2.6 nm and the pore surface was covered by hydroxyl groups. The water flux was 9.8 cc/hr and small salt rejection of 4.7% was observed. After two ALD cycles, the water flux was reduced slightly but the salt rejection increased from

4.7% to 18%, suggesting that the polyamide surface chemistry has a substantial impact on the salt rejection properties. After 4 ALD cycles, water flux was reduced to 4.1cc/hr and the salt rejection approached 40%. At this moment the estimated pore size was about 2.0 nm according to gas permeance data. After 8 cycles, the water flux further reduced to 2.8 cc/hr, and the salt rejection increased to 53%, where the estimated pore size was about 1.2 nm. After 16 cycles, water flux was 2.2 cc/hr, and the salt rejection increased substantially to 78%, where the estimated average pore size was about 2–3 Å, but the relatively low He/N_2 selectivity of 16 suggests that there may be open defects in the membrane at this point. After 32 cycles, the water flux slightly decreased to 2.0 cc/hr, while the salt rejection increased to 86%. The estimated average pore size was still around 2–3 Å, but the higher He/N_2 selectivity indicates a lower defect level. The water flux did not diminish much even though the thickness of the ALD layer doubled. This suggests that after 32 cycles the ALD membrane is thin enough that membrane thickness is not the limiting factor for water transport.

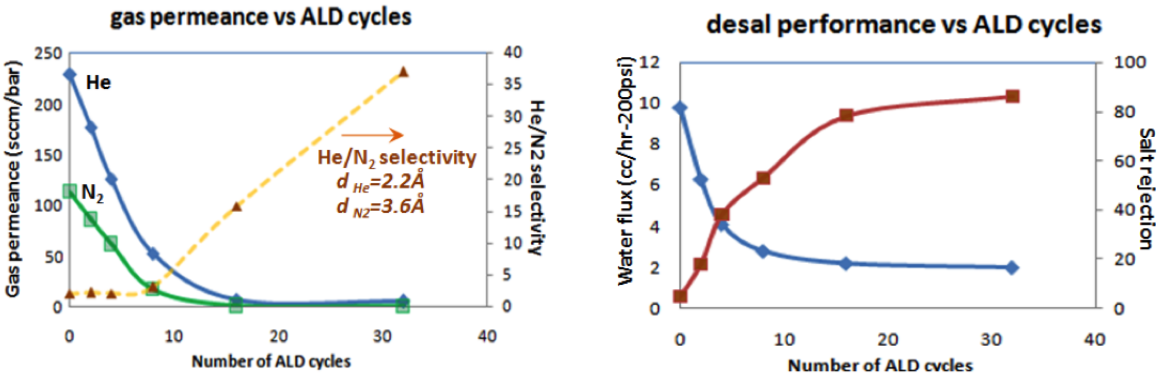

(a) Gas permeance and He/N_2 selectivity

(b) Water flux (blue) and salt rejection (red).

Figure 4.3. Variation of membrane characteristics with increasing number of ALD cycles

Four more samples were prepared with 32 ALD cycles. The water flux was measured to be 2.00, 2.10, 2.00, and 2.18 cc/hr and the salt rejections were all in the range of 85%-95%. Fig. 4.4 shows a performance comparison between this ALD membrane and a sample FILMTEC^{TM} SW30HR membrane tested under the same conditions. Compared to the polyamide thin film composite (TFC) membrane, the ALD membrane has around three times the water flux at 300 psi, and the ratio increases with decreasing pressure. The salt rejection ratio for the ALD membrane is slightly lower than the commercial DOW membrane at the high pressure for which the SW30HR membrane was designed. At 150 psi, the ALD membrane does well in both water flux and salt rejection. In addition, the ALD membrane still retains a linear flux relationship and nearly constant salt rejection with decreasing pressure, making it able to operate highly efficiently as low as 80 psi (at only 26 psi of resistive loss), where it achieves a flux of $l_P = 3.05$ cm/h·bar and 87% salt rejection – for a standard resistance of $\epsilon = 0.16$ bar·h/cm!

In this work, we have demonstrated the fabrication of high flux desalination membranes

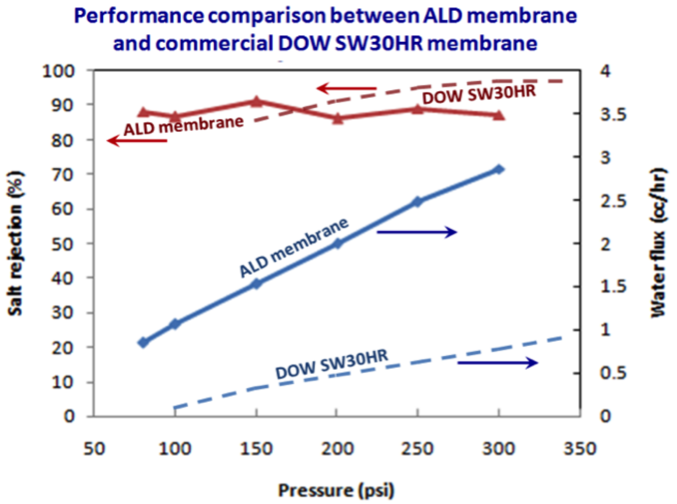

Figure 4.4. Comparison between ALD membrane and commercial DOW membrane

with substantial salt rejection capabilities based on a hybrid inorganic/organic framework. The combination of self-assembled mesoporous silica and subsequent ALD tuning has permitted synthesis of an oriented nanoporous geometry with which it is possible to mimic some features of natural water channels. The immediate improvement in salt rejection after 2 ALD cycles hints that the mixed amide/hydrophobic surface chemistry plays an important role in ion exclusion. Further cycles substantially increase the salt rejection, likely through a combination of narrowing the channel diameter and defect healing. When the average channel size is narrowed to atomic dimensions, 2–3 Å in diameter, 85 95% salt rejection is achieved.

With current processing conditions, our membrane may contain gap defects requiring more ALD cycles to close, blocking some smaller pores in the process. Despite this shortcoming, the high flux rates achieved show that active pores remain very good water conductors. Such chemically tunable membranes allow strong tests of channel structure/function relationships to lay the groundwork for future desalination technologies using nano-engineered structures. The low-pressure desalination performance of the present membrane shows that a breakthrough is possible in membrane energy efficiency using oriented porous materials.

Other important design goals for reverse osmosis membrane materials include a broader operating pH and temperature range and reduced susceptibility to oxidation, biological attack and degradation. Although there is plenty of room at the nano-scale for innovations of the membrane support to address these these considerations, they must eventually be taken into account before nanoporous reverse osmosis membranes can be brought to fruition.

Some of the advantages of silica-based membranes are the high thermal stability and material strength of silicates, the negligible observed dependence of rejection rate on feed pressure, and the ability to control pore interior independently from surface chemistry. The latter property could prove highly useful in further development of surface chemistries to prevent biofouling. Indeed, biofilm formation on silica surfaces has been considered before in the biomedical literature. Silica is known to be much more tolerant to high temperatures than polymer membranes, and this can be exploited for controlling microorganisms by sterilization. Although our anodisk®-based membrane has not been able to show the high burst strength required for seawater desalination, the pore structure itself is expected to be much less compressible than polymer membranes, resulting in higher water flux during high pressure operation. Additionally, our system does not show reduced salt rejection at low pressure operation as in conventional polymer membranes. Finally, the large range of potential pore modifications makes this an ideal setup for achieving fine-grained control over the solute rejection characteristics of ultra low pressure, nanofiltration membranes.

Chapter 5

Conclusions

In this project, we have completed a range of theoretical and experimental studies to understand, design, implement, and test novel nanoporous reverse osmosis membrane materials. Investigations of ion selectivity in biological systems have helped elucidate the principles of ionic selectivity encountered by natural water conducting and ion-selective channels and generate possibilities for their translation into synthetic pores. Based on our achievements in atomic layer deposition (ALD) and molecular imprinting techniques, we have constructed structures that mimic biological pores in dimensions and exposed functionality. Their atomic-scale was demonstrated using gas molecule size selectivity, and several have been shown to possess improved salt rejection and water permeability.

Significant accomplishments have been made toward developing a science-based understanding of the principles for optimization of water flux and select salt rejection in membranes. Both equilibrium and non-equilibrium desalination energy requirements were derived in a form suitable for application to industrial processes, revealing the critical impact of the membrane water permeability on overall process energy requirements and the potential ≈25% decrease on total energy consumption that could be made possible through future improvements in membrane technology. We have completed computational studies of pressure-driven water and salt permeation through model nanopore membranes, with both dipolar walls and chemically decorated/undecorated mouths. We found that, in contrast to experience with polymer membranes, for fixed channel dimensions *lower* salt rejection is observed with very high applied pressure, even for decorated pore mouths, which highlights the importance of ion pairing effects. Through an examination of model dipolar membranes, we found several important electrostatic mechanisms for ion selection. Theoretical studies of cation selective biological channels revealed that selectivity can be achieved through either flexible pore binding sites that over-coordinate the permeant ion or through maintaining a specific cavity size chemically preferred by the permeant ion. Simulations on coarse-grained membrane models showed that the negative dipole moments of oxygens lining both silica and potassium channel pores cause cations to populate the pore interior more strongly for longer pores, with corresponding anion exclusion. Next, water occupying regions of the pore far from the center (where the surface dipole is changing and the electric field is largest) are unable to provide screening at large distances, lowering the effective dielectric of the pore interior to values in the neighborhood of 2.3 to 10 for 12 nm pores[16]. Because of the long-ranged interaction of permeating ions with the oppositely oriented membrane surface dipoles, different dipole densities on the pore interior and membrane surface are required to achieve a net electrostatic potential in macroscopic pores. Salt rejection was found to be much higher for pores incorporating uniform dipole layers along the channel as opposed to simple functionalization of the outer pore rim. Atomistic molecular dynamics calculations with hydrophobic pores showed smaller diffusion constants, indicating lower water permeabilities, correlating with experimentally observed lower flux and higher salt rejection. Ab-initio molecular dynamics simulations also identified the structural origins of the dual-acidity constant behavior observed at silica-water interfaces. This acid-base behavior governs the net charge inside silica pore membranes, which affects desalination performance through tuning the channel's ionic selectivity and hydrophilicity. These theoretical works have made valuable contributions to the design and testing of new desalination membrane materials and processes.

We have also made advancements in technical and experimental capabilities and expertise for nanoporous membrane design, fabrication, testing and application. Using liquid-phase atomic layer deposition, we achieved deposition of biomimetic chemical functionality on self-assembled mesoporous silica to create 2-3 nm nanopores capable of high salt rejection and water permeability. The best measurements on these systems yielded standardized resistances of 0.16 bar-h/cm, two to three times lower than the lowest energy consumption membranes currently available for brackish water desalination. This efficiency increase would directly translate to a 50-66% decrease in operating energy loss at each RO membrane unit. These membranes are capable of constant salt rejection at very low excess pressure and are in addition relatively insensitive to input salt concentration for salinities in the useful operating range above 0.05 mol/L (Fig. 3.9(a)). Preliminary capacitance measurements of plain 2.6 nm diameter silica pores placed the interior dielectric around 29, roughly consistent with the theoretical estimates on narrower channels. Also in accord with theory, but contrary to expectations of decreased friction from pore walls, increases in pore hydrophobicity decreased water permeability. Although the increase in water contact angle and water-pore surface tension should imply decreased pore wetting and friction, a combination of decreased pore size by the dewetted trimethylsilyl groups and water orientational restriction have combined to produce this result. Finally, experiments to understand the role of surface charge on ion transport through nanopores with pore sizes smaller than the Debye screening length have resulted in new insights into water reactions at the silica-water interface. Because of the multiple protonation reactions of surface silanols, we measured the surface charge of silica as a function of pH, and found that the isoelectric point of nanoporous silica is pH=3∼4, 0.5∼1.5 higher than a flat silica surface. The combination of theory and experiment utilized in this project has thus given both top-down and bottom-up characterizations of the utility and chemistry of these novel nanoporous membrane materials.

The studies undertaken in this work lay the groundwork for research in several future directions. First, preliminary work has shown that an extension of the nonequilibrium theory of Chapter 2 to account for electrically driven transport can be developed. This will enable determination of individual ion selectivities and water flux through voltage measurements on patches of tens of nanochannels. Studying batch to batch variations at this reduced size will allow us to separate out irreproducible fluxes arising from membrane defects as well as lead to further information on ion transport behavior within nanopores. This approach has not yet been pursued to completion due to possible difficulties in inferring the very small water flux through these small patches from variations in current with time and concentration[30, 33], and in addition is not suitable for scale-up.

Next, the phenomenal conductivity of aquaporins and the theoretical limiting conductivity calculated in Chapter 2 indicates that order of magnitude improvements in water permeabilities over what has been achieved to date are still possible. Since this report has shown improved flux and salt rejection capabilities, the most pressing need is to develop a strong, flexible support containing a high density of oriented nanochannels for ALD modification. This can provide a work-around for the brittle anodized alumina supports used in Chapter 4 – required for creating ideal porous structures matching theoretical studies used to learn pore design rules – and possibly decrease the number of large gap defects. It would also enable incorporation of the resulting membrane into the spiral wound elements common to industrial operations and possibly ALD deposition in an assembly line format. Further improvements enabling the placement of water-coordinating groups at precise intervals along the channel axis would allow an even closer approach to the aquaporin structure, bringing further possible improvements in performance.

Finally, the approach taken in this work for ALD functionalization of nanochannels can be immediately applied in other important energy storage and separation applications. Carbon dioxide capture and removal could potentially be mediated by pores able to transport carbonate selectively. Further incorporating a switchable gate into such a CO_3^{2-}-selective pore would provide a membrane capable of novel staged architectures for CO_2 separation. Our biologically inspired approach also holds potential promise for the study and design of novel Li^+-selection mechanisms for translation into synthetic membranes. Ion selective membranes in general can be used to convert energy stored in concentration gradients directly into electrical energy.

Our experiments show that the behavior of ions confined within nanopores differ significantly from that in free bulk solutions. Our theoretical studies show novel structural designs that control ion passage through membranes. Based on these observations, new ideas have been developed to help design nanopores that permit fast transport of water and select ions, thus providing novel solutions for energy-efficient, highly selective membrane-based separation technology critical not only to water purification, but also pertinent to electrical energy storage applications in supercapacitors and lithium-ion batteries. Our work thus strongly impacts Sandia's missions in national energy security (efficient separations) and public health (clean, cheap water).

References

[1] W. T. Andrews, W. F. Pergande, and G. S. McTaggart. Energy performance enhancements of a 950 m^3/d seawater reverse osmosis unit in Grand Cayman. *Desalination*, 135(1–3):195–204, 2001.

[2] D. Asthagiri, P. D. Dixit, S. Merchant, M. E. Paulaitis, L. R. Pratt, S. B. Rempe, and S. Varma. Ion selectivity from local configurations of ligands in solutions and ion channels. *Chem. Phys. Lett. (Frontiers Article)*, 485(1–3):1–7, 2010. (invited, cover page).

[3] Z. Chen and Y. B. et al. Jiang. Dna translocation through an array of kinked nanopores. *Nature Materials*, 9:667–675, 2010.

[4] R. T. Cygan, C. J. Brinker, M. Nyman, K. Leung, and S. B. Rempe. A molecular basis for advanced materials in water treatment. *MRS Bull.*, 33:42–47, 2008.

[5] F. Fornasiero, H. G. Park, J. K. Holt, M. Stadermann, C. P. Grigoropoulos, A. Noy, and O. Bakajin. Ion exclusion by sub-2-nm carbin nanotube pores. *Proc. Nat. Acad. Sci.*, 105(45):17250–17255, 2008.

[6] J. Bernard Heymann and Andreas Engel. Aquaporins: Phylogeny, structure, and physiology of water channels. *News Physiol. Sci.*, 14(5):187–193, 1999.

[7] C. Jarzynski and O. Mazonka. Feynman's ratchet and pawl: An exactly solvable model. *Phys. Rev. E*, 59(6):6448–6459, Jun 1999.

[8] E. T. Jaynes. The minimum entropy production principle. *Ann. Rev. Phys. Chem.*, 31:579–601, 1980.

[9] Y.-B. Jiang, G. Xomeritakis, Z. Chen, D. Dunphy, D. Kissel, J. L. Cecchi, and C. Jeffrey Brinker. Sub-10 nm thick microporous membranes made by plasma-defined atomic layer deposition of a bridged silsesquioxane precursor. *J. Amer. Chem. Soc.*, 129:15446–15447, November 2007.

[10] Ying-Bing Jiang, Nanguo Liu, Henry Gerung, Joseph L. Cecchi, and C. Jeffrey Brinker. Nanometer-thick conformal pore sealing of self-assembled mesoporous silica by plasma-assisted atomic layer deposition. *J. Amer. Chem. Soc.*, 128(34):11018–11019, 2006.

[11] Peter C. Jordan. Tuning a potassium channel–the caress of the surroundings. *Biophys. J.*, 93(4):1091–1092, 2007.

[12] L. Kastelan-Kunst, V. Dananic, B. Kunst, and K. Kosutic. Preparation and porosity of cellulose triacetate reverse osmosis membranes. *J. Membrane Sci.*, 109(2):223–230, 1996.

[13] C. T. Kresge, M. E. Leonowicz, W. J. Roth, J. C. Vartuli, and J. S. Beck. Ordered mesoporous molecular sieves synthesized by a liquid-crystal template mechanism. *Nature*, 359:710–712, 1992.

[14] R Kubo. The fluctuation-dissipation theorem. *Rep. Prog. Phys.*, 29:255, 1966.

[15] Uri Lachish. Osmosis and thermodynamics. *Am. J. Phys.*, 75(11):997–998, 2007.

[16] K. Leung. Ion-dipole interactions are asymptotically unscreened by water in dipolar nanopores, yielding patterned ion distributions. *JACS*, 130:1808, 2008.

[17] K Leung, I. M. B. Nielsen, and L. J. Criscenti. Elucidating the bimodal acid-base behavior of the water-silica interface from first principles. *J. Amer. Chem. Soc.*, 131(51):18358–18365, 2009.

[18] K. Leung and S. B. Rempe. Ion rejection by nanoporous membranes in pressure-driven molecular dynamics simulations. *J. Comput. and Theor. Nanosci.*, 6:1–8, 2009. (invited).

[19] K. Leung, S. B. Rempe, and A. von Lilienfeld. Ab initio molecular dynamics calculation of ion hydration free energies. *J. Chem. Phys.*, 130(20):204507–204518, 2009.

[20] Kevin Leung, Susan B. Rempe, and Christian D. Lorenz. Salt permeation and exclusion in hydroxylated and functionalized silica pores. *Phys. Rev. Lett.*, 96(9):095504, Mar 2006.

[21] Ira N. Levine. *Physical Chemistry.* McGraw-Hill, 5th ed. edition, 2001.

[22] Liangxiong Li, Junhang Dong, and Tina M. Nenoff. Transport of water and alkali metal ions through mfi zeolite membranes during reverse osmosis. *Sep. Purif. Tech.*, 53(1):42–48, 2007.

[23] Liangxiong Li, Junhang Dong, Tina M. Nenoff, and Robert Lee. Desalination by reverse osmosis using MFI zeolite membranes. *J. Membr. Sci.*, 243(1-2):401–404, 2004.

[24] David R. Lide. *CRC Handbook of Chemistry and Physics.* CRC Press, Boca Raton, FL, 2004.

[25] C. D. Lorenz, M. Tsige, S. B. Rempe, M. Chandross, M. J. Stevens, and G. S. Grest. Simulation study of the silicon oxide and water interface. *J. Comput. and Theor. Nanosci.*, 2010. (invited, in print).

[26] Yan-Yue Lu, Yang-Dong Hu, Xiu-Liung Zhang, Lian-Ying Wu, and Qing-Zhi Liu. Optimum design of reverse osmosis system under different feed concentration and product specification. *J. Membr. Sci.*, 287(2):219–229, 2007.

[27] S. Moghaddam, E. Pengwang, and Y. B. et al. Jiang. An inorganic-organic proton exchange membrane for fuel cells with a controlled nanoscale pore structure. *Nature Nanotech*, 5:230–236, 2010.

[28] A. W. Mohammad, N. Hilal, H. Al-Zoubi, and N. A. Darwish. Prediction of permeate fluxes and rejections of highly concentrated salts in nanofiltration membranes. *J. Membr. Sci.*, 289(1-2):40–50, 2007.

[29] Kazuyoshi Murata, Kaoru Mitsuoka, Teruhisa Hirai, Thomas Walz, Peter Agre, J. Bernard Heymann, Andreas Engel, and Yoshinori Fujiyoshi. Structural determinants of water permeation through aquaporin-1. *Nature*, 407:599–605, October 2000.

[30] Tatsuhiro Okada, Signe Kjelstrup Ratkje, and Harald Hanche-Olsen. Water transport in cation exchange membranes. *J. Membrane Sci.*, 66(2-3):179–192, 1992.

[31] Shaowei Ong, Xiaolin Zhao, and Kenneth B. Eisenthal. Polarization of water molecules at a charged interface: second harmonic studies of the silica/water interface. *Chemical Physics Letters*, 191(3-4):327 – 335, 1992.

[32] Lars Onsager. Reciprocal relations in irreversible processes. I. *Phys. Rev.*, 37(4):405–426, Feb 1931.

[33] Magnar Ottøy, Tormod Førland, Signe Kjelstrup Ratkje, and Steffen Møller-Holst. Membrane transference numbers from a new emf method. *J. Membrane Sci.*, 74(1-2):1–8, 1992.

[34] G. Owen, M. Bandi, J. A. Howell, and S. J. Churchouse. Economic assessment of membrane processes for water and waste water treatment. *J. Membrane Sci.*, 102:77–91, 1995.

[35] J. Pang, J. N. Stuecker, Y.-B. Jiang, A. J. Bhakta, E. D. Branson, P. Li, J. Cesarano, D. Sutton, P. Calvert, and C. J. Brinker. Directed aerosol writing of ordered silica nanostructures on arbitrary surfaces with self-assembling inks. *SMALL*, 4(7):982–989, 2008.

[36] G. Pique. Low power bill makes desalination affordable. *Int't Desal. And Water Reuse Quarterly*, November 2005.

[37] S. B. Rempe and K. Leung. Response to "comment on 'ab initio molecular dynamics calculation of ion hydration free energies' [jcp 133, xx71xx (2010).". *J. Chem. Phys.*, 133(1), 2010. (in print).

[38] S. B. Rempe, T. R. Mattsson, and K. Leung. On the complete basis set limit and plane-wave methods in first-principles simulations of water. *Phys. Chem. Chem. Phys. (Communication)*, 10:4685–4687, 2008.

[39] R. Riley. *Reverse Osmosis.* 1990. vol. 2, US DOE Report DOE/ER/30133-H1.

[40] Dow Water & Process Solutions. *FILMTEC^{TM} Reverse Osmosis Membranes Technical Manual.* Dow Chemical Company, Midland MI. electronic resource, downloaded Sept. 2010.

[41] A. J. Staverman. Non-equilibrium thermodynamics of membrane processes. *Trans. Faraday Soc.*, 48:176–185, 1952.

[42] R. L. Stover. Energy recovery device performance analysis. ERI Technical Report, 2005.

[43] R. L. Stover. Low energy consumption SWRO. ERI Technical Report, 2008.

[44] Emad Tajkhorshid, Peter Nollert, Morten ø Jensen, Larry J. W. Miercke, Joseph O'Connell, Robert M. Stroud, and Klaus Schulten. Control of the selectivity of the aquaporin water channel family by global orientational tuning. *Science*, 296(5567):525–530, April 2002.

[45] S. Varma and S. B. Rempe. Tuning ion coordination architectures to enable selective partitioning. *Biophys. J.*, 93:1093–1099, 2007.

[46] Sameer Varma and Susan B. Rempe. Structural transitions in ion coordination driven by changes in competition for ligand binding. *J. Am. Chem. Soc.*, 130(46):15405–15419, 2008.

[47] Sameer Varma and Susan B. Rempe. Multi-body effects in ion binding and selectivity. *Biophys. J.*, 2010. in press.

[48] Sameer Varma, Dubravko Sabo, and Susan B. Rempe. K^+/Na^+ selectivity in K channels and valinomycin: Over-coordination *versus* cavity-size constraints. *J. Mol. Biol.*, 376:13–22, 2008.

[49] Troy W. Whitfield, Sameer Varma, Edward Harder, Guillaume Lamoureux, Susan B. Rempe, and Benoît Roux. Theoretical study of aqueous solvation of K^+ comparing ab initio, polarizable, and fixed-charge models. *J. Chem. Theory Comput.*, 3(6):2068–2082, 2007.

[50] G. Xomeritakis, N.G. Liu, Z. Chen, Y.-B. Jiang, R. Khn, P.E. Johnson, C.-Y. Tsai, P.B. Shah, S. Khalil, S. Singh, and C.J. Brinker. Anodic alumina supported dual-layer microporous silica membranes. *J. Membrane Sci.*, 287(2):157–161, 2007.

[51] Luning Zhang, Seema Singh, Chuanshan Tian, Y. Ron Shen, Yan Wu, Mark A. Shannon, and C. Jeffery Brinker. Nanoporous silica-water interfaces studied by sum-frequency vibrational spectroscopy. *J. Chem. Phys.*, 130(15):154702, 2009.

DISTRIBUTION:

1 Ying-Bing Jiang
E PS, MSC03 2040
1 University of New Mexico
Albuquerque NM 87131-0001

2	MS 0895	S. Rempe, 08635
2	MS 1315	D. M. Rogers, 08635
1	MS 1413	E. Ackerman, 08635
1	MS 9291	B. Simmons, 08630
1	MS 9161	B. Even, 08650
1	MS 9161	S. Allendorf, 08656
1	MS 9405	G. Kubiak, 08600
1	MS 0754	M. Rigali, 06736
1	MS 1415	P. J. Feibelman, 01130
1	MS 0886	T. M. Alam, 01816
1	MS 0735	J. Merson, 06730
1	MS 0754	P. Brady, 06730
1	MS 0484	R. Hwang, 08004
1	MS 1427	C. Barbour, 01100
1	MS 1315	J. Nelson, 01130
1	MS 0724	J. Hruby, 06000
1	MS 0899	Technical Library, 9536 (electronic copy)
1	MS 0161	Legal Intellectual Property, 11500
1	MS 0359	D. Chavez, LDRD Office, 1911

v1.35

Sandia National Laboratories